A Linear Equivalent Barotropic Model of the Antarctic Circumpolar Current with Realistic Coastlines and Bottom Topography

ALEXANDER KRUPITSKY,* VLADIMIR M. KAMENKOVICH,+ NAOMI NAIK, AND MARK A. CANE

Lamont-Doherty Earth Observatory, Columbia University, Palisades, New York

ABSTRACT

A linear equivalent barotropic (EB) model is applied to study the effects of the bottom topography H and baroclinicity on the total transport and the position of the Antarctic Circumpolar Current (ACC). The model is based on the observation of Killworth that the time mean velocity field of the FRAM Model is self-similar in the vertical.

A realistic large-scale topography $\bar{H}$ is constructed by filtering 5-minute resolution data with an appropriate smoothing kernel. It is shown that the asymptotic behavior of the solution of the barotropic model (a particular case of the EB model) in the limit of very small bottom friction depends on subtle details of topography and basin geometry. Given the uncertainties of the smoothing procedure the authors conclude that the barotropic model is not robust with respect to possible variations of model topography.

The authors found that the EB model with a vertical profile function similar to that of Killworth reproduces the major features of the time- and depth-averaged FRAM solution, including the position and the transport of the ACC, reasonably well. The solution is robust with respect to uncertainties in $\bar{H}$. The EB model is much improved by a parameterization of the bottom friction via near-bottom velocity, which tends to shut off the flow in the shallow regions.

1. Introduction

The purpose of this work is to develop a simple wind-driven model describing the depth-averaged flow in the Antarctic Circumpolar Current (ACC) region.[1] The primary objective of the model is to study the influence of bottom topography and baroclinicity on the total transport and the position of the ACC.

The ACC is a strong eastward current encircling the Antarctic continent with a mean transport of about 130 Sv (Whitworth 1983). It is bounded by the Subtropical Front (except in Drake Passage) on the equatorial side and by the poleward edge of the Upper Circumpolar Deep Water on the poleward side (Orsi et al. 1995). There are no apparent external constraints that dictate the position of the ACC axis. The maximum of westerlies driving the ACC is situated well to the north of Drake Passage. This appears to be the main reason for a general southern drift in the ACC. To the east from

Drake Passage the current abruptly turns northward forming a western boundary current (the Malvinas Current). This is, in the essence, the scheme suggested by Stommel (1957), where the global scale deviations of the ACC from the zonal path are determined by the location of the continents and by the wind stress field. The bottom topography must be the primary reason for the observed smaller scale meridional deviations of the ACC.

It has long been noticed that topography seems to steer the ACC on certain parts of its path, notably over the zonally oriented midocean ridge in the southwestern Pacific (e.g., Gordon et al. 1978). At the same time, the flow appears to be less affected by the meridionally oriented topographic features. Even such a major obstruction as the Kerguelen Plateau forces only a part of the current to the north where one would expect the whole flow to turn, had it been barotropic. The branch of the ACC associated with the southern ACC front circumvents the Kerguelen Plateau from the south, implying a great deal of baroclinic compensation.

The deviations of the ACC from the zonal path due to the influence of topography were analyzed in the early linear barotropic models by Ivanov and Kamenkovich (1959) and Kamenkovich (1962). (More recent linear barotropic models are reviewed in section 4.) Thompson (1971) suggested that the intensification of the ACC over the northern flank of a zonally oriented ridge can be caused by upgradient transfer of momen-

---

* Current affiliation: Woods Hole Oceanographic Institution, Woods Hole, Massachusetts.

+ Current affiliation: P. P. Shirshov Institute of Oceanology, Russian Academy of Sciences, Moscow, Russia.

[1] Preliminary results of this work were reported in Kamenkovich et al. (1994).

Corresponding author address: Dr. Alexander Krupitsky, Woods Hole Oceanographic Institution, Woods Hole, MA 02543.

tum by eddies. McCartney (1976) and Smith and Fandry (1978) attributed this feature to crowding of f/H contours (f being the Coriolis parameter, H the ocean depth) over the northern slope. Eddy-resolving numerical experiments using two-layer quasigeostrophic models by McWilliams et al. (1978) and Wolff and Olbers (1989) showed the intensification of the current over the northeastern slope of a localized seamount. The Wolff and Olbers (1989) model ACC exhibited very large deviations from a zonal path over a high meridional ridge.

The early attempts to model the ACC as a current over a flat bottom led to excessive transport, which could only be controlled by assuming huge lateral viscosities (e.g., Hidaka and Tsuchiya 1953). Munk and Palmen (1951) were the first to hypothesize that it is topographic pressure drag (the resultant pressure force acting against submarine hills and troughs) that balances the input of momentum by the wind stress. Using the results of FRAM, D. Stevens and V. Ivchenko (1994, unpublished manuscript) and Killworth and Nanneh (1994) found that the major part of the zonal momentum input by the wind within the latitude belt of the Drake Passage is balanced by topographic pressure drag. Thus, topography significantly affects not only the path but also the momentum balance in the ACC. It should be noted, however, that these balances may differ from that of the ACC itself (Ivchenko et al. 1996). The reason is that the ACC deviates significantly from a purely zonal path and action of pressure forces on the lateral boundaries of the ACC may be noticeable.

The dependence of the magnitude of the ACC transport on the bottom topography was extensively studied using global barotropic models with "realistic" relief. Il'in et al. (1969, 1974) considered a linear barotropic model with bottom friction as the only mechanism of dissipation. With the coefficient $r = 7.7 \times 10^{-7} \text{ s}^{-1}$ ($r = \varepsilon/H$ in the notation of section 2) they found transports of 51 Sv and 43 Sv ($\text{Sv} \equiv 10^6 \text{ m}^3 \text{ s}^{-1}$) in the constant depth and realistic depth cases, respectively. It is likely that the difference would be larger if the coefficient r were taken smaller. Laykhtman et al. (1971) integrated the barotropic streamfunction equation with a modified bottom friction parameterization for the global ocean with realistic depth distribution. The flow was forced by the wind stress derived from monthly atmospheric pressure fields. They found an average ACC transport of 350 Sv with seasonal variations from 248 Sv in December to 434 Sv in July. Bryan and Cox (1972), using the GFDL homogeneous global ocean model, calculated ACC transport to exceed 650 Sv in the case of a flat bottom. The essential dissipation used was Laplacian lateral friction with coefficient $A_H = 4 \times 10^4 \text{ m}^2 \text{ s}^{-1}$. The transport decreased to 32 Sv when realistic topography was introduced. Bye and Sag (1972) reported a substantial difference between the ACC transport in the constant and variable depth cases

of their numerical model with bottom friction coefficient r of order 10^{-6} s^{-1}: 358 and 177 Sv, respectively. They also found that in the variable depth case the effect of the frictional processes on the circumpolar circulation was of minor importance.

The wide scatter in magnitude of the ACC total transport calculated using different barotropic models is apparent. We argue that this is to some extent due to the different models using different large-scale bottom topographies. Our hypothesis is that much of the scatter results from uncertainties in the large-scale topography $\bar{H}$. This conjecture will be supported by the results presented in sections 4 and 5.

It is generally accepted practice to use large-scale components of the relief $\bar{H}$ for the modeling of the large-scale ocean circulation. In this connection two questions arise: First, how to define the large-scale component $\bar{H}$ of the bottom topography if we know the real depth H at each location with sufficient accuracy. The concept of "large-scale component" is intuitively clear, but it is hardly possible to define it uniquely. Then one should consider not only the influence of $\bar{H}$ but also the robustness of the results with respect to some perturbations $\delta\bar{H}$. A somewhat related problem of the influence of uncertainties in the forcing field was studied by Schröter and Wunsch (1986). The issue of robustness, however, of model results with respect to the bottom topography does not seem to be addressed in the current literature. We will discuss it in section 3.

Second, it is possible that the small-scale component of the topography $H' = H - \bar{H}$ cannot be completely neglected. For example, H' could generate small-scale components of velocity $\mathbf{u}'$ and then the "Reynolds stresses," $\overline{\mathbf{u}' \cdot \nabla H'}$, could generate large-scale motion. Scaling arguments suggest that such terms may be important (Bogden et al. 1993). Based on analysis of the FRAM output, Grose et al. (1995) argued that smoothing the bottom topography leads to an increase by about 50 Sv of the total transport of the ACC, as compared to the observations.

One of the most comprehensive modeling efforts to date to study the dynamics of the ACC in their full complexity is the Fine Resolution Antarctic Model Project (FRAM Group 1991). An eddy-resolving model with 32 vertical levels is used to assimilate climatological data to produce dynamically consistent fields of temperature, salinity, and velocity. While FRAM appears to reproduce satisfactorily many of the known features in the Southern Ocean, the sensitivity studies with such a model are prohibitively expensive.

The nonrobustness of barotropic models and the complexity of the general circulation models like FRAM have been a motivation for us to build a model of a different type, more suitable for the intended process-oriented studies. Analysis of the FRAM results (Killworth 1992) showed that the time-mean velocity field in the ACC is close to self-similar in the vertical, that is, the flow at one depth is both parallel and proportional

to the flow at another depth. While the correlations between the velocity fields on different levels somewhat deteriorate with depth, they mostly remain above 0.5 for both u and v components, an "observational" fact which we find quite remarkable. We do not address the question of formation of such equivalent barotropic (EB) structure in this study but simply take it as a given. This ansatz enables us to construct the EB model described in section 2. Equivalent barotropic models are widely known in atmospheric sciences since the application to numerical weather forecasting by Charney and Eliassen (1949). Shtockman (1950) used a similar approach to estimate the density distribution in the ocean from the known depth-averaged velocity field.

In studying the effects of bottom relief and baroclinicity on the transport and the position of the ACC, an EB model has the advantage over a general circulation model of allowing many variations in model parameters. In addition, an analytical treatment of some typical cases may be obtained, adding to our understanding of the ACC behavior. The familiar barotropic model is a particular case of the EB model. A somewhat related study was recently undertaken by Marshall (1995) who assumed that potential vorticity is a linear function of density.

Although Killworth (1992) put forward a simple theory predicting the existence of the EB structure on isopycnal surfaces for a wide variety of situations, it still remains unclear how the EB structure is established and what the conditions for its existence are. For instance, in the idealized eddy-resolving numerical experiments by Wolff and Olbers (1989) a meridional ridge (case $R3$) seems to have destroyed much of the self-similarity.

The paper is organized as follows. The model is described in section 2. The averaging of the topographic data and a discussion of resulting $\bar{H}$ and potential vorticity fields is given in section 3. The numerical solutions for the case of a β-plane channel with an idealized topography are presented in section 4. The solutions for the realistic geometry and topography are discussed in section 5. We conclude with a brief summary in section 6. Numerical methods for solving problems considered in sections 4 and 5 are outlined in appendix B.

2. The model

Neglecting horizontal viscosity and nonlinear terms, the steady momentum equations on a β plane are written as

$$-fv = \frac{\partial p'}{\partial x} + A_v \frac{\partial^2 u}{\partial z^2} \qquad (1)$$

$$fu = \frac{\partial p'}{\partial y} + A_v \frac{\partial^2 v}{\partial z^2}, \qquad (2)$$

where x, y, and z are directed eastward, northward, and upward, respectively; u, v are the zonal and meridional velocity components, respectively; f is the Coriolis parameter; $p' = p/\rho_0$, p is the pressure and A_v is the vertical viscosity coefficient. In accord with the result of Killworth (1992), we assume

$$\nabla_H p' = g(\nabla_H \xi) P(z). \qquad (3)$$

Here $\xi P(0)$ is the unknown sea level and $P(z)$ is the prescribed vertical profile function. Representation (3) is the cornerstone of our model. Integrating (1) and (2) in the vertical yields

$$-fV = -gF \frac{\partial \xi}{\partial x} + \tau_x - \tau_x^b \qquad (4)$$

$$fU = -gF \frac{\partial \xi}{\partial y} + \tau_y - \tau_y^b, \qquad (5)$$

where g is the acceleration due to gravity; τ_x and τ_y (τ_x^b and τ_y^b) are the zonal and meridional components of the wind (bottom) stress (divided by the mean density ρ_0), respectively;

$$\mathbb{U} = (U, V) = \int_{-H}^{0} (u, v) dz;$$

$$F(H) = \int_{-H}^{0} P(z) dz.$$

Here H is the depth.

We assume that bottom friction is proportional to near-bottom velocities ($\tau_b \sim \mathbf{u}_b$). Ansatz (3) then allows the parameterization

$$\tau_b = (\tau_b^x, \tau_b^y) = \varepsilon \mathbb{U} \frac{P(-H)}{F(H)}, \qquad (6)$$

where ε is the constant bottom friction coefficient.

Assuming $P(z) \equiv 1$ reduces this model to a conventional barotropic model where $F(H) = H$.

Equations (4) and (5) are supplemented by the vertically integrated continuity equation

$$\frac{\partial U}{\partial x} + \frac{\partial V}{\partial y} = 0. \qquad (7)$$

The system (4), (5), and (7) constitutes the equivalent barotropic (EB) model. The parameters of the model are the friction coefficient ε and the profile function $P(z)$.

We assume that the lateral boundary of the Southern Ocean consist of two closed curves Γ_S and Γ_N: Γ_S is the southern boundary, that is, the Antarctic continent, and Γ_N consists of the boundary of the South American continent and some zonally oriented fluid boundary. The boundary conditions are

$$(\mathbb{U} \cdot \mathbf{n}) = 0 \quad \text{at } \Gamma_S,$$

$$(\mathbb{U} \cdot \mathbf{n}) = \begin{cases} 0 & \text{at solid part of } \Gamma_N \\ U^{\Gamma} & \text{at fluid part of } \Gamma_N, \end{cases} \qquad (8)$$
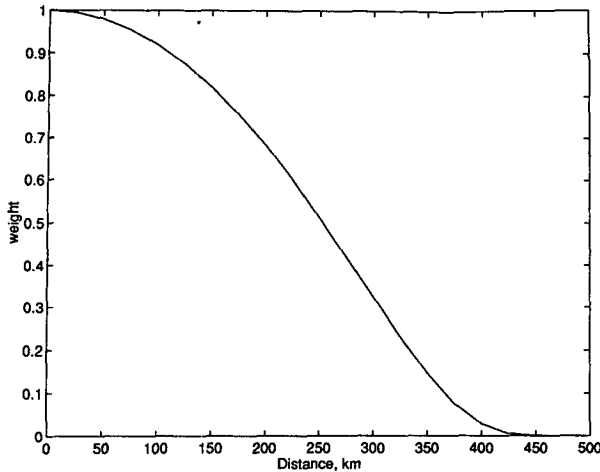
FIG. 1. Normalized weight in (23) $\exp\{-\alpha r^2/[R^2(R^2 - r^2)]\}$ as a function of distance r, $R = 500$ km, $\alpha = 2R^2$.

where U^{Γ} is a specified function and $\mathbf{n}$ is the unit normal to the boundaries Γ_S and Γ_N; between the boundaries of South America $\int U^{\Gamma} dx = 0$.

We introduce the transport streamfunction ψ:

$$U = -\frac{\partial \psi}{\partial y}, \quad V = \frac{\partial \psi}{\partial x}.$$

Dividing (4), (5) by $F(H)$ and taking the curl yields the potential vorticity equation

$$\varepsilon \left[\frac{\partial}{\partial x} \left(\frac{P(-H)}{F^2} \frac{\partial \psi}{\partial x} \right) + \frac{\partial}{\partial y} \left(\frac{P(-H)}{F^2} \frac{\partial \psi}{\partial y} \right) \right]$$
$$+ J\left(\psi, \frac{f}{F} \right) = \operatorname{curl}_z \frac{\tau}{F}, \quad (9)$$

where

$$J(A, B) = \frac{\partial A}{\partial x} \frac{\partial B}{\partial y} - \frac{\partial A}{\partial y} \frac{\partial B}{\partial x},$$

$$\operatorname{curl}_z \mathbf{A} = \frac{\partial A_y}{\partial x} - \frac{\partial A_x}{\partial y}.$$

The boundary conditions for ψ follow from (8). Using that ψ is determined up to a constant, we have

$$\psi = 0 \quad \text{at } \Gamma_S \quad (10)$$

$$\psi = \begin{cases} T & \text{at solid part of } \Gamma_N \\ T + \psi^{\Gamma} & \text{at fluid part of } \Gamma_N, \end{cases} \quad (11)$$

where

$$\psi^{\Gamma} = -\int U^{\Gamma} dx.$$

The integral is taken along the fluid part of the boundary Γ_N from one continent to another (recall that the total transport between each pair of continents is assumed to be zero).

The constant T is the total transport of the ACC, determined from a constraint

$$\oint_{\Gamma} \left(\frac{f}{F} \frac{\partial \psi}{\partial s} + \varepsilon \frac{P(-H)}{F^2} \frac{\partial \psi}{\partial n} + \frac{\tau_s}{F} \right) ds = 0, \quad (12)$$

which is readily derived from (4) and (5) using the single valuedness of the sea level ξ (Kamenkovich 1961). Here Γ is an arbitrary closed contour that lies within the domain of integration and embraces the Antarctic continent, $\mathbf{s}$ is directed along Γ in a counterclockwise sense, $\mathbf{n}$ is orthogonal to Γ in such a way that $(\mathbf{s}, \mathbf{n}, \mathbf{k})$ constitute the right triplet, where $\mathbf{k}$ is the vertical unit vector.

The EB model is formally equivalent to the usual barotropic model with the quantity f/F playing the role of potential vorticity. Therefore, the results obtained for barotropic models are also fully applicable to EB model.

To solve (9) with the boundary conditions (10)–(12) we represent ψ as

$$\psi = \psi_1 + T\psi_2, \quad (13)$$

where the auxiliary function ψ_1 is the solution of (9) with the boundary conditions

$$\psi_1 = 0 \quad \text{at } \Gamma_s \quad (14)$$

$$\psi_1 = \begin{cases} 0 & \text{at solid parts of } \Gamma_N \\ \psi^{\Gamma} & \text{at fluid parts of } \Gamma_N, \end{cases} \quad (15)$$

and the auxiliary function ψ_2 is the solution of the homogeneous version of (9) with the boundary conditions

$$\psi_2 = \begin{cases} 0 & \text{at } \Gamma_s & (16) \\ 1 & \text{at } \Gamma_N. & (17) \end{cases}$$

The total transport T of the ACC is determined from (12) by substituting (13):

$$T = -\frac{I_1}{I_2} = -\frac{\oint_{\Gamma} \left(\frac{f}{F} \frac{\partial \psi_1}{\partial s} + \varepsilon \frac{P(-H)}{F^2} \frac{\partial \psi_1}{\partial n} + \frac{\tau_s}{F} \right) ds}{\oint_{\Gamma} \left(\frac{f}{F} \frac{\partial \psi_2}{\partial s} + \varepsilon \frac{P(-H)}{F^2} \frac{\partial \psi_2}{\partial n} \right) ds}.$$
$$(18)$$

The auxiliary functions ψ_1 and ψ_2 are the solutions of Dirichlet problems for elliptic differential equations and are uniquely determined. Note that taking the area integral of (9), applying Stokes theorem and using the boundary conditions (14)–(17) shows that integrals I_1 and I_2 are independent of the path of integration. Then, for all Γ closed around Antarctica

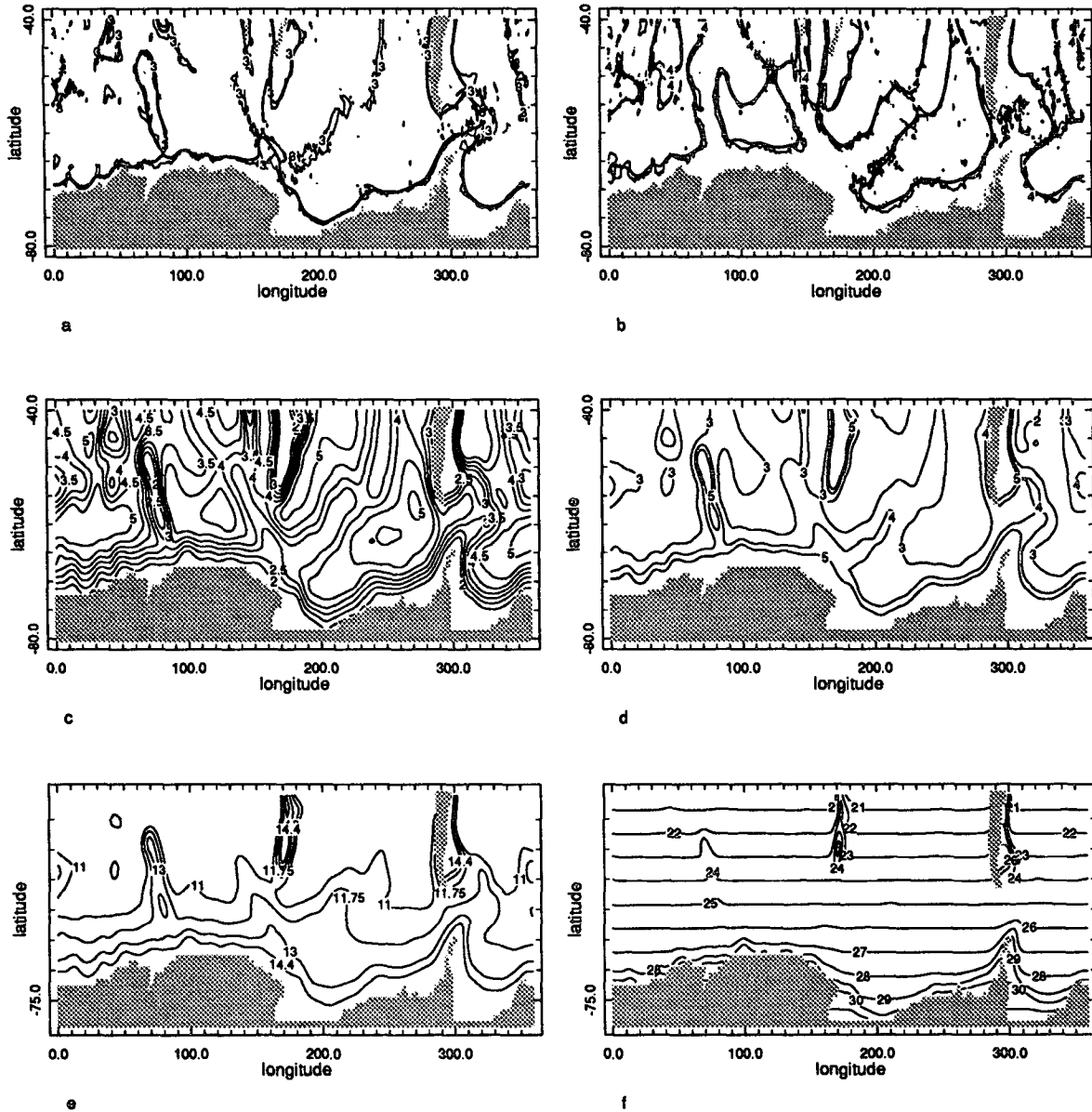$$\frac{\delta I_1}{\delta \Gamma} = \frac{\delta I_2}{\delta \Gamma} = 0. \quad (19)$$

FIG. 2. (a) Smoothed and unsmoothed isobath 3 km for $R = 500$ km, $\alpha = 2R^2$; (b) Smoothed and unsmoothed isobath 4 km, R and α as in (a); (c) Smoothed depth in km, R and α as in (a); (d) Contours of f/H in 10^{-8} m^{-1} s^{-1} corresponding to (c); (e) Contours of f/F in 10^{-8} m^{-1} s^{-1}, $c_\infty = 0.05$, $H_0 = 900$ m; (f) Contours of f/F in 10^{-8} m^{-1} s^{-1}, $c_\infty = 0$, $H_0 = 500$ m.

Parameter ε is poorly estimated and is usually assumed small (the models reviewed in section 1 assume ε of order 10^{-3} m s^{-1}). Fortunately, many features of the solution do not depend on ε, as long as ε is small. For this reason, it is very helpful to find the leading term in the expansion of the solution in an asymptotic series in ε. The first step is to neglect the term with ε in (9) in the interior of the domain of integration. Then we obtain the generalized Sverdrup relation

$$J\left(\psi, \frac{f}{F} \right) = \text{curl}_z \frac{\tau}{F} . \qquad (20)$$

The characteristics of this first-order differential equation are the isolines of the equivalent-barotropic potential vorticity

$$q = f/F = \text{const}. \qquad (21)$$

In the pure barotropic case, $P(z) \equiv 1$, the characteristics of the problem are the familiar f/H isolines.

Consider a cluster of q isolines that intersect the boundary of our region. Generally (20) is valid in the interior of the region, but near the boundary we expect the formation of a Stommel boundary layer. It is easy to show that a boundary layer exists if
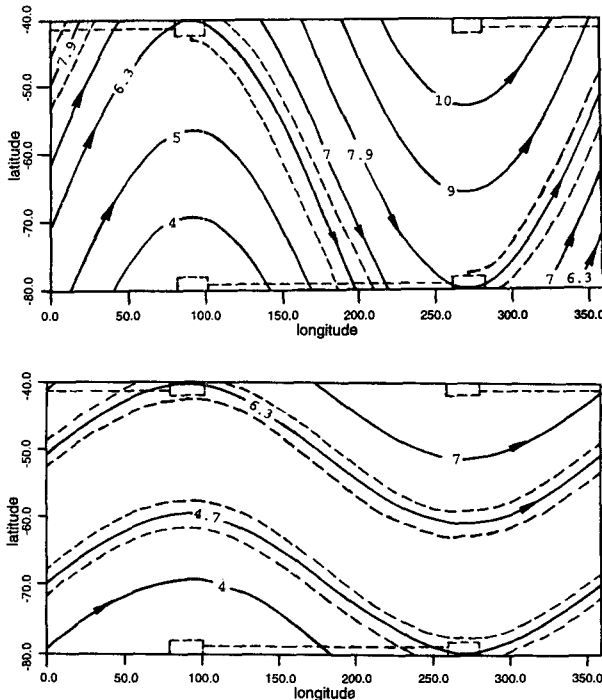
FIG. 3. The schematic of $|q|$ contours (solid) and boundary layers (dashed) corresponding to (25), $q_0 = -3.15$. (a) $\delta = 1.5$; (b) $\delta = 0.5$. The arrows indicate direction of integration.

$$\left(\frac{\partial q}{\partial s}\right)_{\zeta}\Big|_b < 0,\qquad(22)$$

where the coordinates (s, ζ) are such that ζ isolines are parallel to the boundary, s isolines are orthogonal to it with the domain of integration to the left of $(\nabla s)_b$. The subscript b indicates that the function is evaluated at the boundary.

As in the familiar Sverdrup solution, (20) should be integrated along q isolines from the boundary where the boundary layer cannot exist. At this boundary the solution of (20) should satisfy the specified boundary conditions (10) or (11).

If, on the other hand, q isolines are closed around Antarctica, then the asymptotics are completely different. Kamenkovich (1962) showed that to a first approximation the isolines of ψ and q will coincide and ψ will be $O(\varepsilon^{-1})$. Transitional boundary layers of width $O(\varepsilon^{1/2})$ will be formed between the regions where $\psi = O(1)$ and $\psi = O(\varepsilon^{-1})$ (see also Has'minskii 1962; Gill 1968). A brief derivation of asymptotic expansions for a simple model case with closed q contours is given in appendix A.

The asymptotics demonstrate in the most distinct way that the value of the ACC transport depends crucially on the geometry of the q contours. We turn now to the determination of these isolines in the Antarctic region.

Note that the location of boundary layers becomes intuitively clear if (9) is viewed as the advection–diffusion equation for ψ with the streamfunction f/F.

3. Determination of the large-scale bottom topography

As we have discussed already, there is no ultimate method to determine the "real" large-scale topography. The standard approach is to apply some kind of averaging to the original topographic data to filter out small-scale structures and to preserve large-scale features.

To smoothly map available topographic data (5' × 5' resolution Navy database ETOPO5) to an arbitrary grid we use the procedure suggested by Il'in et al. (1974). Let x, y be a point where we wish to find the smoothed depth $\bar{H}$ (large-scale component of H). Then

$$\bar{H}(x, y) = \frac{\sum_{r_i^2 < R^2} H(Q_i)\exp\left(-\frac{\alpha}{R^2 - r_i^2}\right)}{\sum_{r_i^2 < R^2}\exp\left(-\frac{\alpha}{R^2 - r_i^2}\right)},\qquad(23)$$

where $Q_i = x_i, y_i$ is a node of the original grid, $H(Q_i)$ is the depth at the point Q_i, $r_i^2 = (x_i - x)^2 + (y_i - y)^2$, α and R are parameters. The summation in (23) extends over all points with nonzero depth. The function $\bar{H}(x, y)$ is defined everywhere and is smooth and continuous. Differentiating (23) with respect to x and y yields explicit exact formulas for the derivatives of $\bar{H}$ (Il'in et al. 1974). These are needed to solve (9) numerically. The parameters R and α are chosen to provide reasonable smoothing for the scales that are characteristic for the real ocean. After a number of tests with small-scale (of order 100 km) perturbations superimposed on a large-scale sinusoidal topography, we chose the following values: $R = 500$ km, $\alpha = 2R^2$. Figure 1 shows how the weight decreases with distance from (x, y).

Figures 2a,b illustrate how the method performs. The vast majority of small-scale features of the original map do not exist in the smoothed field and the smoothed isobaths generally follow the mean paths of their counterparts in the unsmoothed field. The notable exception is the absence of the smoothed 3-km isobath representing the East Pacific Ridge in the original data. Being relatively narrow, the East Pacific Ridge has become deeper as a result of smoothing and is represented by the isobath 3.5 km in Fig. 2c.

A smoothed topography for the whole circumpolar region to the south of 40°S is shown in Fig. 2c, with islands (including New Zealand) submerged to 500 m before smoothing for simplicity. All the prominent large-scale structures (midocean ridges, abyssal plains, trenches) are reproduced. The picture is dominated by features of the 10° length scale. The corresponding map
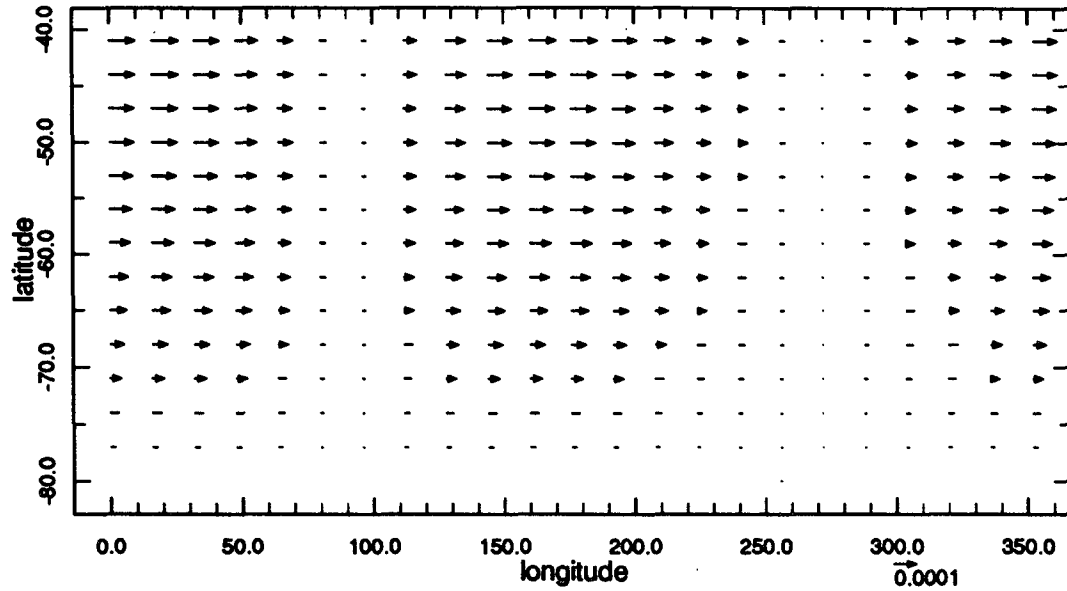
FIG. 4. Zonal wind stress (in N m^{-2}) for idealized topography cases.

of $f/\bar{H}$ contours is shown in Fig. 2d. There are several large closed $f/\bar{H}$ contours associated with well-known topographic features: the Agulhas Plateau, Kerguelen Plateau, South Indian abyssal plain, and the triple juncture of midocean ridges in the South Atlantic.

Inspecting Fig. 2d, one observes that there is a narrow band of closed $f/\bar{H}$ contours around Antarctica. However, these closed contours pass very close to the Antarctic coast at Cape Ann near 50°E. For brevity, we

call this location A_c. The smoothing algorithm near shore entails additional choices that in essence decide how to tell ocean from land in the smoothed field. With different reasonable choices the band of closed $f/\bar{H}$ contours can be wider or narrower or can disappear completely. We cannot objectively determine whether these closed $f/\bar{H}$ contours really exist.

We pose the following question: Is the ACC transport predicted by the barotropic model robust with re-
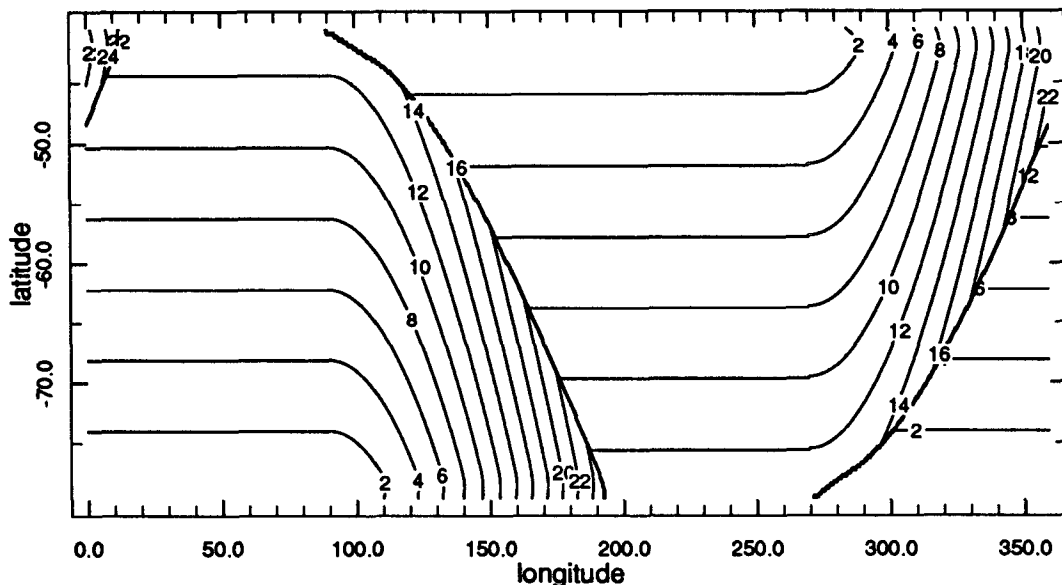

FIG. 5. The solution to (26) for $\delta = 1.5$ (in Sv). (Sverdrup solution); q and τ are given by (25) and (27), respectively.
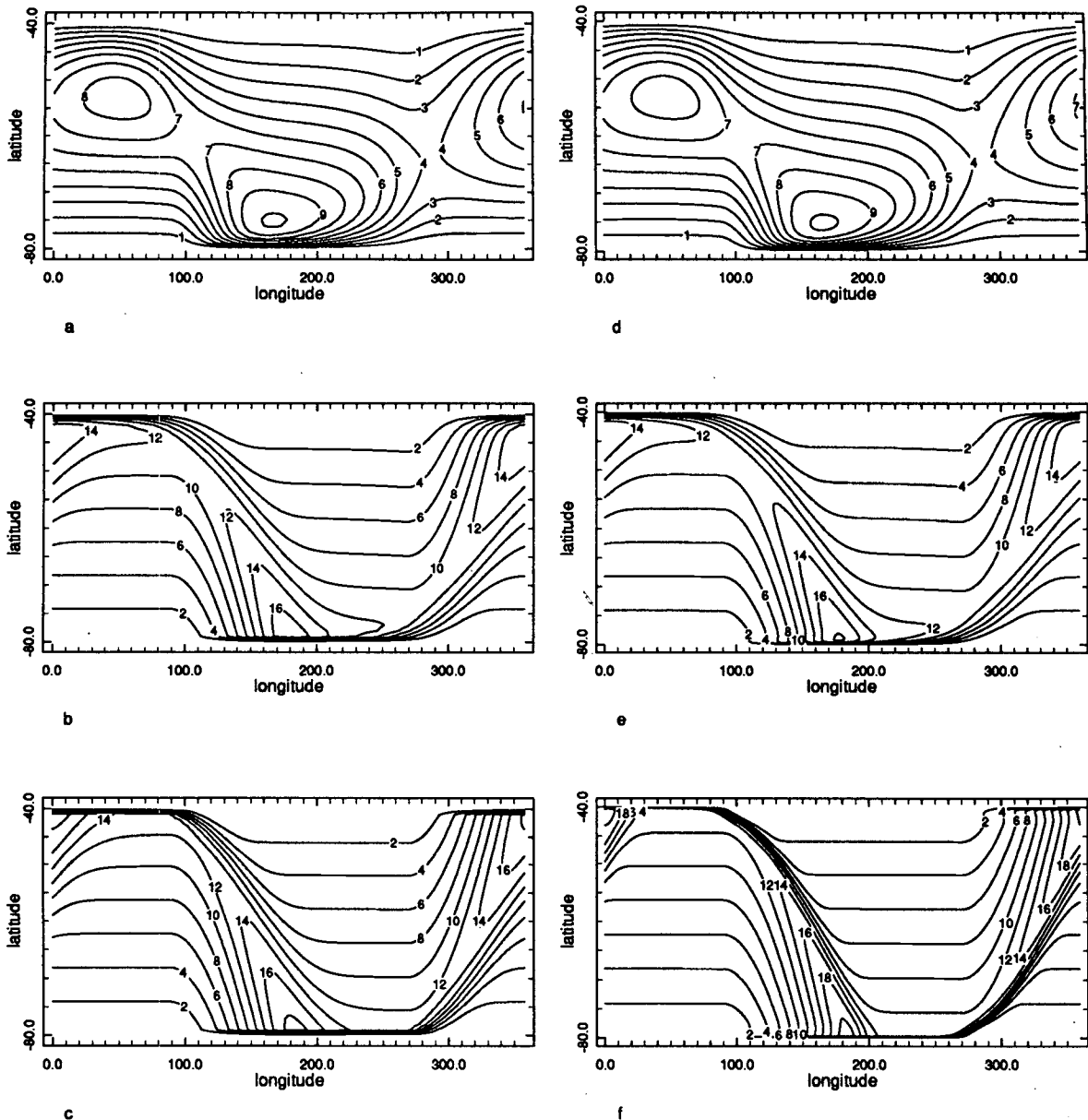
FIG. 6. The numerical solutions for the function ψ_1 (Sv) for various grids and ε. $\delta = 1.5$; q and τ are as in Fig. 5. (a) $2° \times 1°$, $\varepsilon = 10^{-2}$ m s^{-1}; (b) $2° \times 1°$, $\varepsilon = 10^{-1}$ m s^{-1}; (c) $2° \times 1°$, $\varepsilon = 10^{-4}$ m s^{-1}; (d) $1/2° \times 1/4°$, $\varepsilon = 10^{-2}$ m s^{-1}; (e) $1/2° \times 1/4°$, $\varepsilon = 10^{-3}$ m s^{-1}; (f) $1/2° \times 1/4°$, $\varepsilon = 10^{-4}$ m s^{-1}.

spect to perturbations of model geometry? To address this question we perturb the geometry near Cape Ann by artificially adding a small (about 100 km long) peninsula at A_c. We refer to the perturbed model geometry as case B and the unperturbed geometry is case C. The narrow band of $f/\bar{H}$ contours, which are closed in Fig. 2d (case C), are all blocked by addition of the artificial peninsula in case B. Recalling that for small ε the solution to (9) is crucially dependent on the structure of $f/\bar{H}$ contours, we expect quite different behaviors in

cases B and C. This conjecture is examined by numerical experiments in the following sections.

The EB model, on the other hand, is expected to be more robust because $F(H)$ depends more weakly on H. The vertical profile function $P(z)$ found by Killworth (1992) is approximated by

$$P(z) = c_\infty + e^{z/H_0}, \qquad (24)$$

where c_∞ and H_c are some parameters that characterize $P(z)$. In the following we choose $c_\infty = 0.05$, $H_0 = 900$

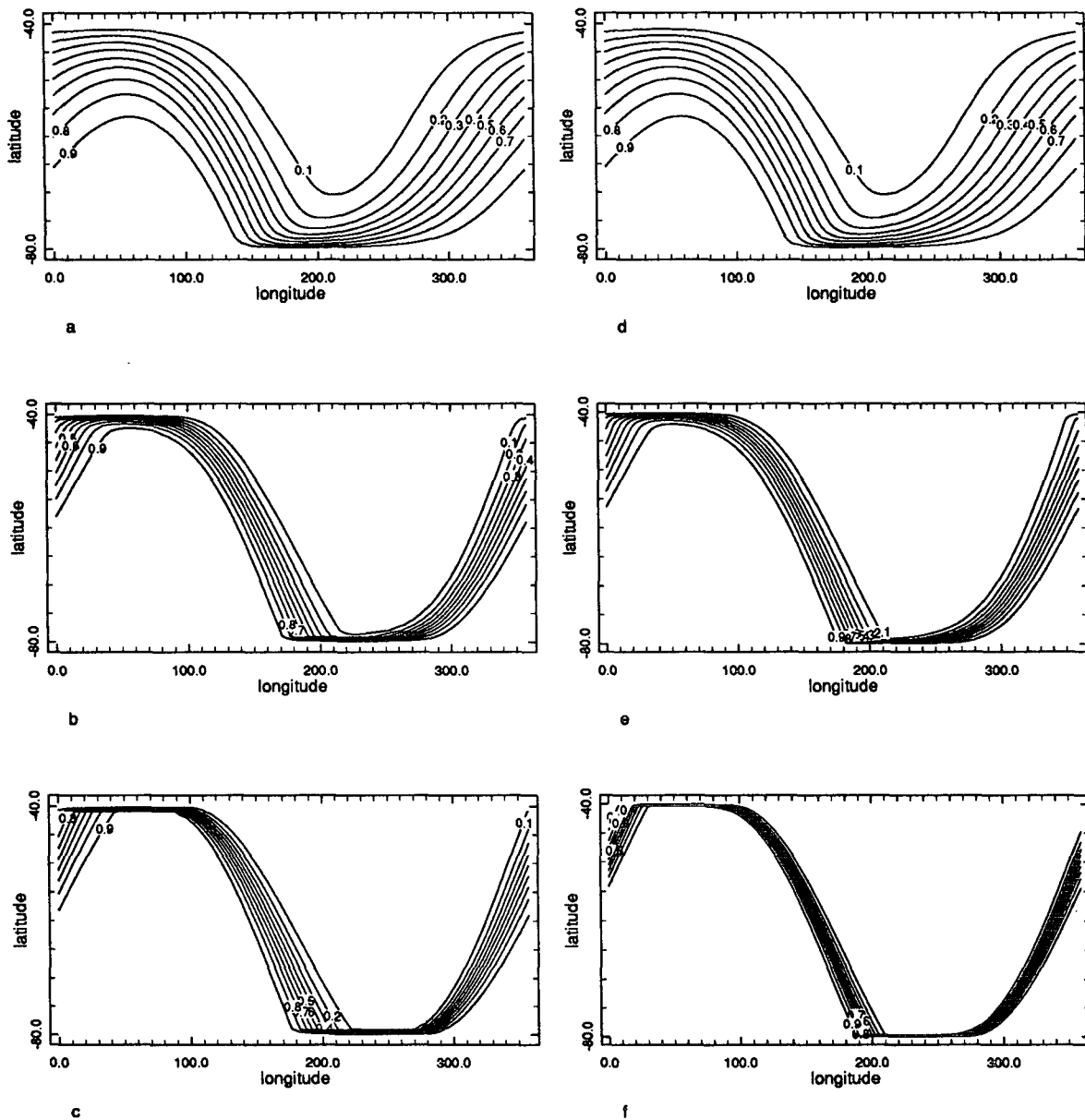SEPTEMBER 1996

KRUPITSKY ET AL.

FIG. 7. As in Fig. 6 but for ψ_2.

m as the most appropriate values. These parameters allow a broad band of characteristics $q = f/F$ circumnavigating the Antarctic continent (Fig. 2e). Note that, if $P(z)$ tends to zero very rapidly with depth, then the dependence of F on H is negligible so that q contours almost coincide with latitude circles, as in a flat bottom model (e.g., see Fig. 2f showing q for $c_\infty = 0$, $H_0 = 500$ m).

4. Cases with an idealized topography

The key question of circumpolar dynamics is what balances the input of momentum and vorticity by wind.

Based on the arguments presented in section 2, one expects the solution to be fully determined by the pattern of q isolines rather than by the geometry of the coast lines or by the details of wind forcing. In the early models of the ACC developed by Kamenkovich (1960, 1962), Gill (1968), and Johnson and Hill (1975) it was assumed that some contours of potential vorticity q close around Antarctica. Such a configuration effectively stipulates the breakdown of the Sverdrup balance in the circumpolar domain. Since the pressure gradient cannot build up on the closed contour, the friction, no matter how small the
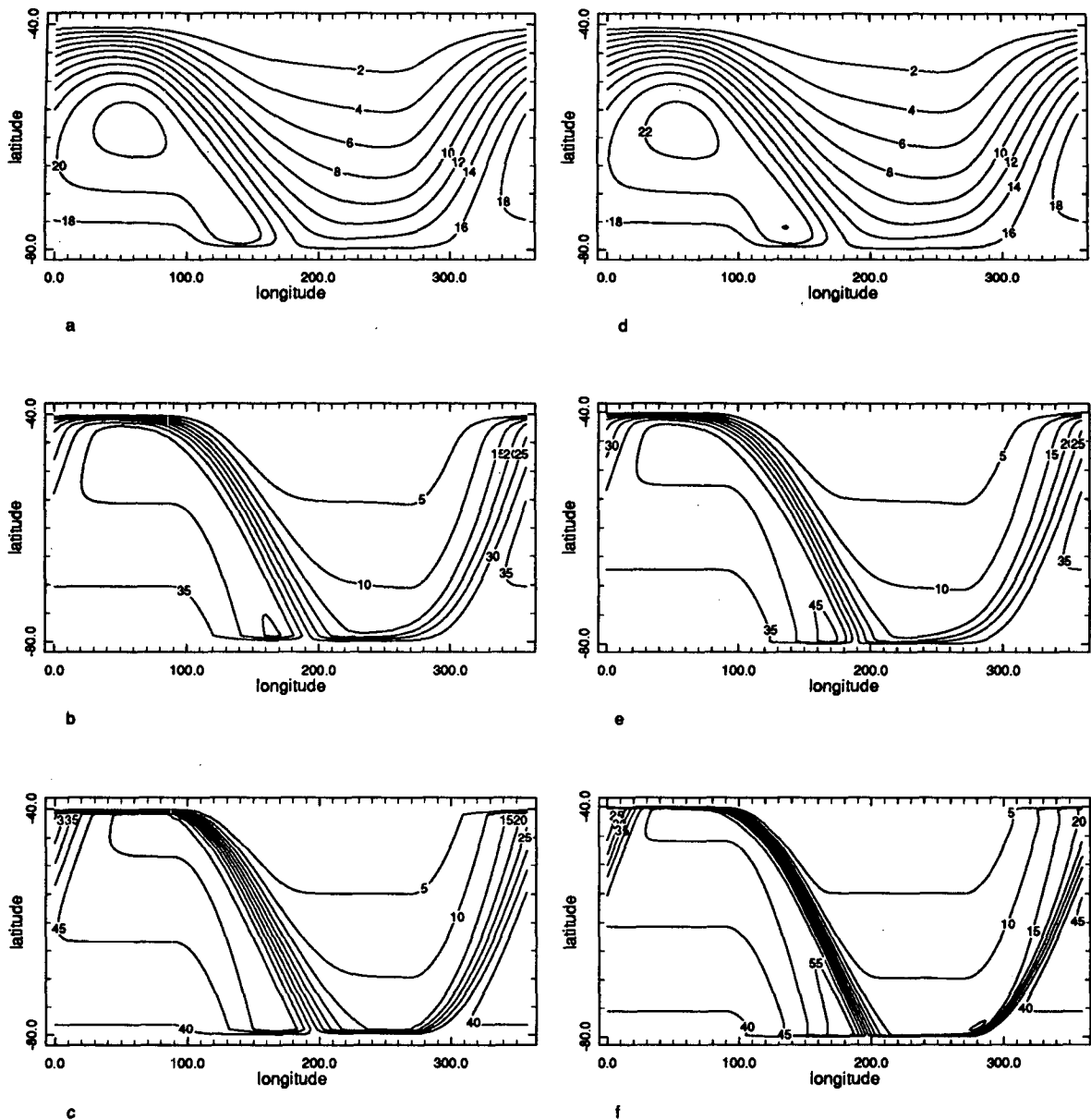
FIG. 8. As in Fig. 6 but for the streamfunction ψ.

coefficient, must balance the wind input. Consequently, the solution varies inversely with the friction coefficient.

The other possibility was studied by Krupitsky and Cane (1994). They considered nearly inviscid wind-driven flow in a zonal channel with the large-scale piecewise linear topographic relief sufficiently high so that all q contours are blocked by the sidewalls. They found that the zonal transport in the channel is independent of friction, similar to the Sverdrup transport in a basin. Certain parts of the sidewalls act as "quasi-western" boundary layers where the circulation closes. A similar study was conducted by Wang and Huang

(1995). Results for domains of a more general shape are reported by Wang (1994), Krupitsky (1995), and Ishida (1994).

To investigate the fundamental properties of the EB model and to select and test the numerical scheme (see appendix B) we begin with an idealized configuration. The ACC is represented as a current in a periodic zonal channel on a β plane ($0 \leqslant x \leqslant L_x$, $0 \leqslant y \leqslant L_y$) with vertical walls: Γ_S is $y = 0$, Γ_N is $y = L_y$, $\psi^\Gamma = 0$ [cf. (10), (11)]. The domain dimensions are chosen to be relevant to the Southern Ocean: $360° \times 40°$; the wind stress will be specified below [cf. (27)]. For conve-

TABLE 1. The transport T (Sv) and its standard deviation σ (T) for the case $\delta = 1.5$; q and τ are given by (25) and (27), respectively.

ε (m s^{-1})	$2° \times 1°$		$1/2° \times 1/4°$	
	T	σ (T)	T	σ (T)
10^{-2}	16.0	0.01	16.0	0.001
10^{-3}	31.7	0.3	30.6	0.05
10^{-4}	39.4	0.4	38.5	0.1

nience, instead of specifying H we prescribe the potential vorticity q [cf. (21)] so that

$$q = q_0 \left[1 + \frac{\delta}{2} \left(1 - \sin \frac{2\pi x}{L_x} \right) + \frac{y}{L_y} \right], \quad (25)$$

where q_0 and δ are parameters (Figs. 3a,b).

If $\delta > 1$, all q isolines that lie in the region are blocked by the boundaries (for such isolines $1 \leq q/q_0 \leq 2 + \delta$); if $\delta < 1$ some q isolines (such that $1 + \delta \leq q/q_0 \leq 2$) are closed around Antarctica. We will solve one representative case from each class by considering (9) with the boundary conditions (10)–(12). For simplicity we take $H = (f_0 + \beta y)/q$, $F = H$, so $P(-H)$ can be found from (24).

(a) $\delta > 1$. We start our analysis with the case $\delta = 1.5$. The typical layout of the boundary layers of ψ_1 [the solution to (9) with the conditions (14), (15)] is given in Fig. 3a. (For the function ψ_2 the picture is similar.) The boundary layers are schematically shown by dashed lines. Arrows show the direction of integration along q isolines according to (22). In this case, there are Stommel boundary layers of width $O(\varepsilon)$ near the parts of the boundary $y = 0$ and $y = L_y$ where characteristics end. Furthermore, there are internal boundary layers of width $O(\varepsilon^{1/2})$ and four transitional regions with the scales $O(\varepsilon^{1/3} \times \varepsilon^{2/3})$ associated with matching of internal and Stommel boundary layers and with the termination of the latter. Similar internal boundary layers and transitional regions were analyzed by Kamenkovich and Reznik (1972). A general approach and necessary mathematical proofs for the case analogous to $\delta > 1$ can be found in Il'in (1992, ch. 4).

Outside the boundary layers and the transitional regions, the Sverdrup relation (20) is valid. The equation for the function ψ_1 in the coordinate system q, y reads

$$\left(\frac{\partial \psi_1}{\partial y} \right)_q = \frac{L_x}{\pi \delta q_0} \frac{\mathrm{curl}_z \frac{\tau}{H}}{\cos \frac{2\pi x}{L}}. \quad (26)$$

To simplify the solution of (26) we choose the wind stress to be zonal and such that (Fig. 4)

$$\mathrm{curl}_z \frac{\tau}{H} = \alpha \left| \cos \left(\frac{2\pi x}{L_x} \right) \right|, \quad (27)$$

where $\alpha = -2.3 \times 10^{-14}$ s^{-2}. The wind stress is of a realistic amplitude. Equation (26) can now be easily integrated from the boundary where the boundary layer cannot exist [cf. (22)]. The solution is presented in Fig. 5.

The purpose of the numerical experiments described in this section is to determine how small ε must be for the solution to be close to the asymptotic limit and what grid resolution is required to reproduce all major properties of the solution for given ε. To this end we conduct two series of experiments on $2° \times 1°$ and $1/2° \times 1/4°$ grids for different values of ε.

The numerical solutions for the function ψ_1 on $2° \times 1°$ and $1/2° \times 1/4°$ grids for different values of ε are shown in Fig. 6.

Calculations show that the resolution does not affect the solution outside the boundary layers. Comparison with the Sverdrup solution depicted in Fig. 5, shows that with $\varepsilon = 10^{-3}$ and $\varepsilon = 10^{-4}$ the numerical solutions are very close to the asymptotic limit in the interior. The solutions for the functions ψ_2 and ψ are shown in Fig. 7 and Fig. 8. The evolution of the boundary layers with ε and grid resolution is clearly seen in Fig. 7. The Il'in scheme used here is not intended to yield good results in the internal boundary layers, and our experiments show that for small ε the solution in the internal boundary layers changes very little with ε. On the other hand, the Stommel boundary layers appear to be better described by a fine resolution model. The dependence of the transport on ε is shown in Table 1. In accordance with the results of Krupitsky and Cane (1994) and Krupitsky (1995), the transport tends to a finite value of the order $\tau_0 L_x / f_0$ as $\varepsilon \to 0$. The transport was calculated using (18) on each latitude represented by the grid. Since the numerical scheme does not guarantee that (19) holds exactly, there is a scatter in the values of the transport obtained on different contours. The standard deviation σ of this scatter is a measure of the accuracy of the scheme. In this case $\sigma < 1\%$ of the transport.

(b) $\delta < 1$. The asymptotics in this case were studied by Kamenkovich (1962), Has'minskii (1962), and Gill (1968). The general procedure is outlined in appendix A. The typical layout of the boundary layers of ψ_1 is given in Fig. 3b. (The corresponding picture for ψ_2 is similar.) In addition to the Stommel boundary layers near the parts of the boundary $y = 0$ and $y = L_y$ and four transitional regions (which are similar to the case $\delta = 1.5$), internal boundary layers of width $O(\varepsilon^{1/2})$ will be formed between the regions where $\psi_1 = O(1)$ and $\psi_1 = O(1/\varepsilon)$. The fundamental property of the asymptotic solution that we would like to reproduce numerically is its inverse dependence on ε within the band of closed q contours.

Before we turn to the computationally complicated case $\delta = 0.5$, we first treat a similar problem but with a constant depth and a meridional barrier in the northern half of the basin. Here $P \equiv 1$, $F = H$, $q = (f_o$

$+ \beta y)/H_o$. This problem is much simpler numerically because the q isolines are latitude lines that are aligned with the grid. This problem was analyzed by Gill (1968). The asymptotic solution for ψ_1 in the southern part of the domain where q isolines are closed ($q_s \leq q \leq q_b$) is simply

$$\psi_1 = \frac{\alpha H^4}{\varepsilon \pi \beta^2} (q - q_s)(q - q_b) \qquad (28)$$

(see appendix A), where q_s and q_b are the values of q at the southern boundary and at the southern tip of the barrier, respectively. The internal boundary layer connects (28) with the Sverdrup solution in the northern part of the domain (Gill 1968).

The numerical solution for ψ_1 for the case $\varepsilon = 10^{-4}$ m s^{-1} on a $1/2° \times 1/4°$ grid is shown in Figs. 9a,b. Note that the width of the internal boundary layer is approximately $4°$ (Fig. 9b). Solutions for ψ_1 in the southern
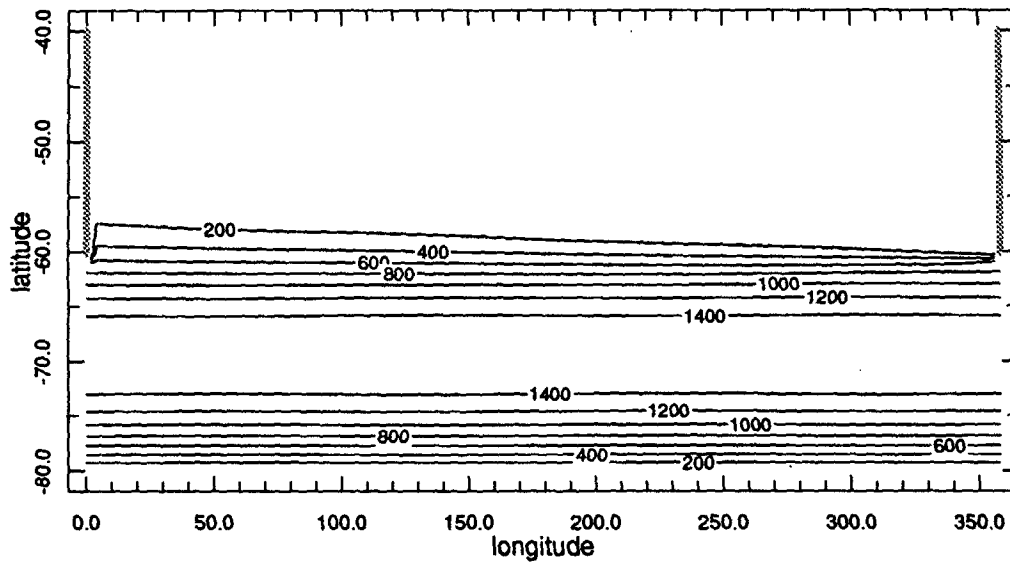
a
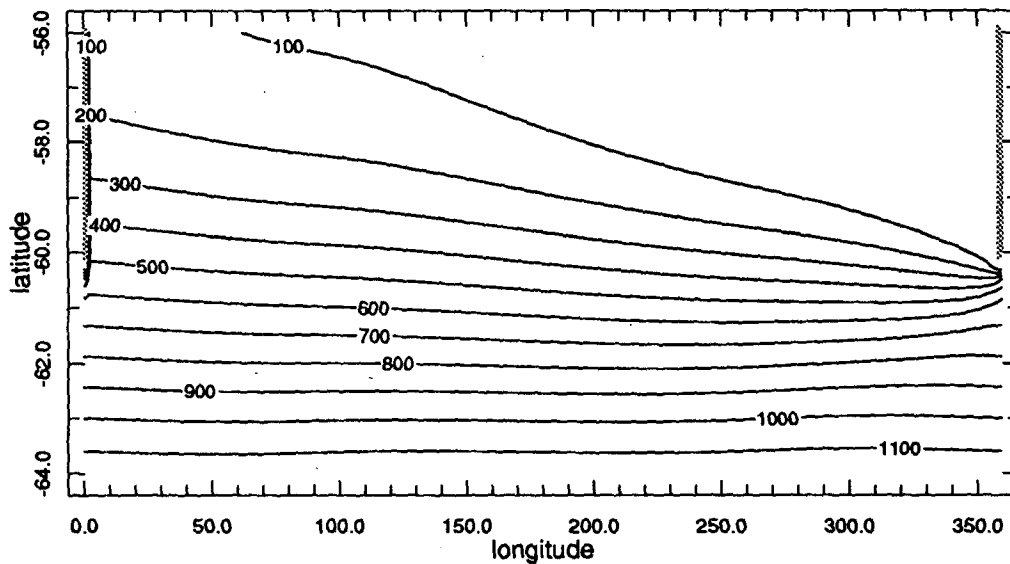
b

FIG. 9. (a) The function ψ_1 (Sv) for the Gill problem, $\varepsilon = 10^{-4}$ m s^{-1}; (b) same as (a) but showing only internal boundary layer; τ is given by (27); H = const. The resolution is $1/2° \times 1/4°$.

part of the domain for different ε are compared with the asymptotic solution (28) in Fig. 10. One observes that the solution with $\varepsilon = 10^{-4}$ m s^{-1} is reasonably close to the asymptotic solution and $\varepsilon = 10^{-5}$ m s^{-1} yields a very good approximation to it. The solution with $\varepsilon = 10^{-3}$ m s^{-1} differs significantly from the asymptotics due to the relatively thick internal boundary layer between the northern and the southern parts.

Now we turn back to the case of q given by (25). The numerical solutions for the streamfunction ψ for δ = 0.5 are shown in Fig. 11. Analysis of the calculated solutions and comparison with the solution on a $1/4°$ $\times$ $1/8°$ grid shows that we approached the asymptotic regime with $\varepsilon = 10^{-4}$ m s^{-1}. The dependence of the transport on the resolution and the scatter of the calculated values of the transport on different latitude lines [cf. (19)] suggests that a $1/2°$ $\times$ $1/4°$ resolution is marginally sufficient for a reliable calculation of the transport for $\varepsilon = 10^{-4}$ m s^{-1} and is certainly sufficient for larger values of ε (Table 2). A comparison of Tables 1 and 2 demonstrates that the required resolution depends not only on the value of the friction coefficient but also, and in a more profound way, on the structure of the field of q isolines. This structure also strongly influences the value of ε at which we approach the asymptotic regime.

5. The case with realistic topography and coastline

a. Barotropic model

We compare the behavior of the solution to (9)–(12) in case B (no q contours closed around Antarctica) with that of case C (a band of closed q contours). Here Γ_S consists of the coast of Antarctica, Γ_N consists of the coast of South America and the latitude line 40°S, $\Psi^\Gamma = 0$. The model was forced by wind stress from Hellerman and Rosenstein (1983). The calculations were performed on grids with the uniform spatial resolution 10 km and 5 km (the latter as a convergence check). From the analysis above we anticipate that the dependence of the total transport on ε would be very different with and without closed q contours. However, in the range of friction parameters where the calculations were feasible ($10^{-4} \leqslant \varepsilon \leqslant 10^{-2}$ m s^{-1}) the solution is far from the asymptotic behavior and the disparity in the calculated ACC transport is less dramatic than in the idealized cases of section 4 (Table 3 and Fig. 12). The most likely explanation is that the band of q contours closed around Antarctica is very narrow, sometimes only about 1° across. From experience with the Gill problem, we expect the internal boundary layers to be a few degrees wide even with $\varepsilon = 10^{-4}$ m s^{-1}. Hence, in our calculations, the band of closed q contours is entirely overlapped by internal boundary layers and we are far from the asymptotic regime where the solution varies inversely with ε.

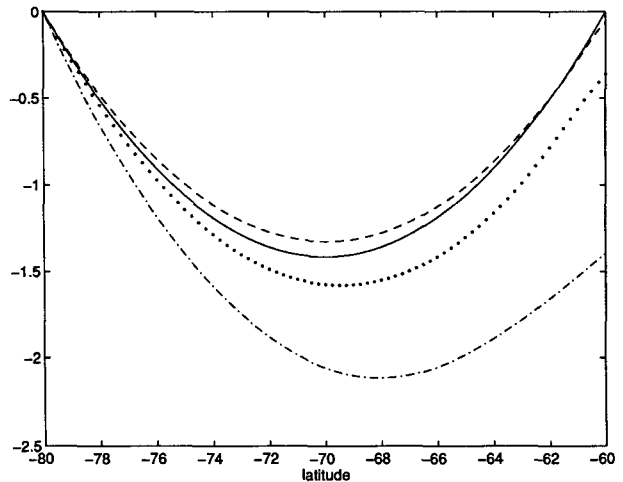In principle, in case C, we could obtain a realistic value of order 130 Sv (Whitworth 1983) with

FIG. 10. Profiles of the function $\varepsilon\psi_1$ (divided by 10^6 m^4 s^{-2}) in the southern part of the domain of the Gill problem: $\varepsilon = 10^{-3}$ m s^{-1} (dash–dotted), $\varepsilon = 10^{-4}$ m s^{-1} (dotted), $\varepsilon = 10^{-5}$ m s^{-1} (dashed), and in the limit $\varepsilon \to 0$ [cf. (28)] (solid). Resolution as in Fig. 9.

$\varepsilon = O(10^{-5}$ m s$^{-1})$ on a finer grid, but this calculation is barely feasible because of the very slow convergence of the iterative process used. In any event, the solution for the ACC would closely follow the q isolines (Kamenkovich 1962; also viz. Fig. 12c) and the location of the ACC would be far from realistic. In addition, the result would not be robust with respect to the presence of the peninsula at A_c. In case B, we observe the blocked regime studied by Krupitsky (1995) where the realistic transport is impossible with any ε, on any grid. The calculated solutions are shown in Fig. 12. For small values of friction the model predicts very strong local recirculations in the regions where the q contours are locally closed. This is explained by the same argument as the too strong ACC with a flat bottom or in the idealized case $\delta = 0.5$. In a more realistic model the wind stress torque acting around closed q contours is likely to be balanced by the baroclinic pressure term (e.g., Welander 1968). Except for the value of the transport, the solutions with $\varepsilon = 10^{-2}$ m s^{-1} look more realistic than the low friction solutions. This suggests that the omitted baroclinic terms are crucial in the momentum and vorticity balances.

Summarizing the results of the last two sections and taking into account the previous efforts referenced in the introduction, we conclude that a linear barotropic model cannot be used for determining the transport and the position of the ACC.

b. An equivalent barotropic model

It may seem that barotropic and EB versions of (9) are almost identical. In fact, however, they differ significantly because the structures of potential vorticity
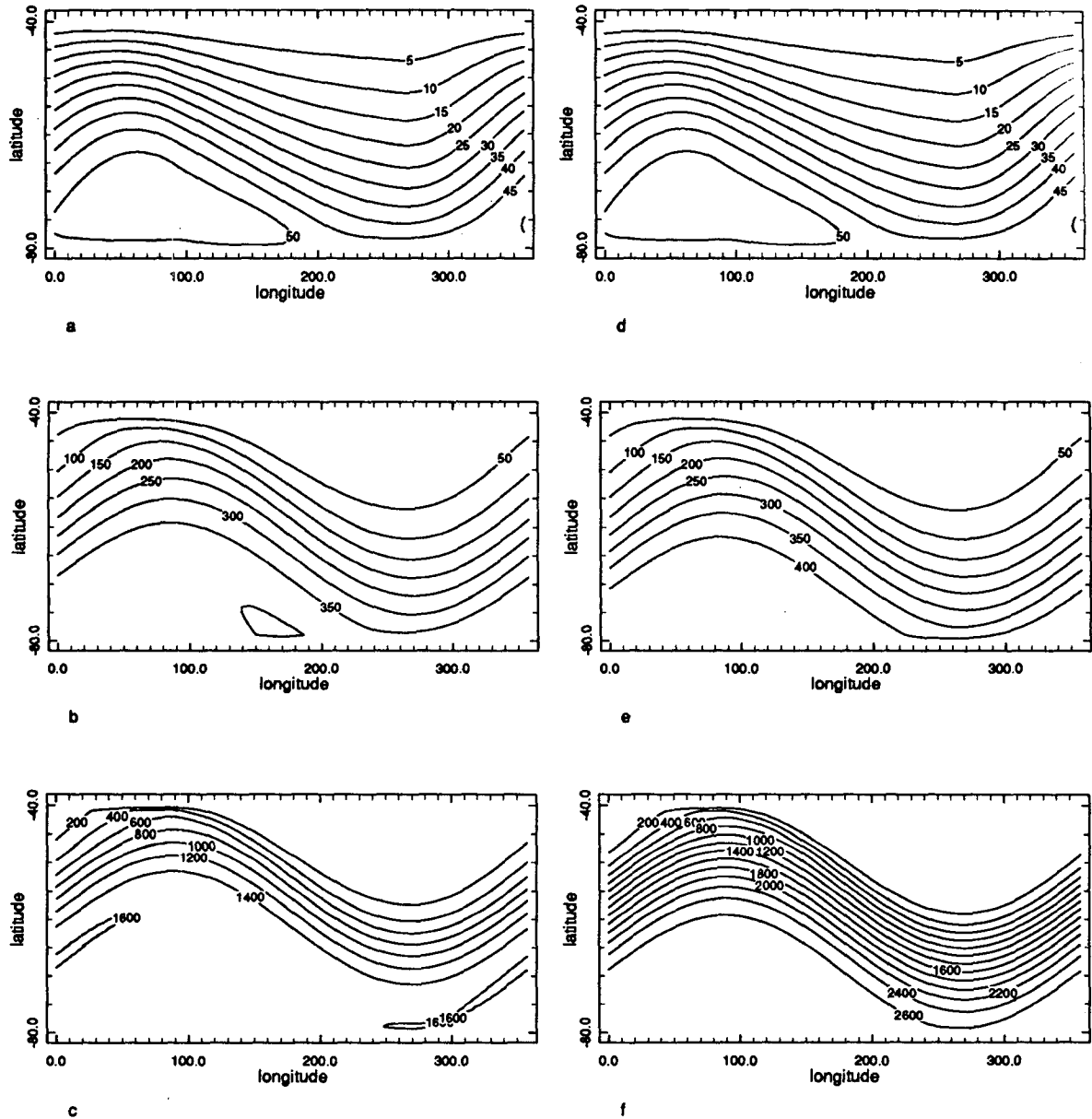
FIG. 11. As in Fig. 8 but for $\delta = 0.5$.

contours are quite different. Recall that nonrobustness of the barotropic model was due to specifics of the geometry of $f/\bar{H}$ isolines where small perturbations in $\bar{H}$ changed the structure of $f/\bar{H}$ contours from the closed case to the blocked. The geometry of f/F contours where a broad band of contours circumnavigates the Antarctic continent (Fig. 2e) is such that small perturbations in $\bar{H}$ do not change their structure. Therefore, the EB model is robust with respect to topographic variations.

The solution of (9), (10)–(12) for $\varepsilon = 10^{-2}$ m s^{-1} (Fig. 13a) is similar in many respects to the time- and depth-averaged solution from FRAM (Fig. 14). In particular, the position of the ACC is satisfactorily reproduced. The resemblance, while considerable, is not totally surprising since the vertical structure (24) reflects the time-mean vertical structure of the FRAM solution. The differences between the two models are concentrated in regions with steep topography, for example, near the southern edge of the Kerguelen Plateau. These discrepancies can be attributed to the violations of the EB assumption (3) in the eddy-energetic areas (Killworth 1992). Our model also fails in the Weddell and Ross gyres where (3) is less likely to hold.

TABLE 2. The transport T (Sv) and its standard deviation σT for the case $b = 0.5$; q and τ are given by (25) and (27), respectively.

ε	$2° \times 1°$		$1/2° \times 1/4°$		$1/4° \times 1/8°$	
	T	$\sigma(T)$	T	$\sigma(T)$	T	$\sigma(T)$
10^{-2}	48.6	0.01	48.6	0.002		
10^{-3}	389	7.6	416	1.5		
10^{-4}	1426	660	2713	286	2701	111

The zonal momentum balances were obtained by averaging (4) within the area bounded by the outermost closed streamlines of the ACC. After integration the Coriolis term vanishes. The integral of the first term of the rhs of (4) yields the resultant pressure force due to topographic pressure drag and due to the action of pressure forces on the lateral boundaries of the ACC. The resultant pressure force on the lateral boundaries is generally not zero because the ACC is not strictly zonal. The integrals of the second and third terms on the rhs of (4) give the contributions of wind and bottom friction. The difference of the latter two terms give the contribution of pressure forces. In this experiment, pressure forces balance 62% of the zonal momentum input from wind in the ACC.

It is interesting to investigate the role of the parameterization of bottom friction via near-bottom velocities (6). We repeated the last experiment (Fig. 13a) replacing (6) by $\tau_b = \varepsilon \bar{u}$ ($\bar{u} = U/H$), which parameterizes bottom friction via the vertically averaged velocity ($\tau_b \sim \bar{u}$), as in the barotropic model. The resulting solution is shown in Fig. 13b. The model ACC now consists of two branches. The southern branch follows the band of closed f/F contours, which brings its path along the southern ACC front (Orsi et al. 1995). Given available observational data, it is difficult to say how realistic this branching is.

Comparison of Fig. 13a and 13b shows that the role of $P(-H)/F$ term is to shut off the flow in the shallow regions. Thus, the southern branch of the ACC mostly flowing over the Antarctic shelf (Fig. 13b) is completely absent in Fig. 13a. Another major difference is observed at the southern edge of the New Zealand Plateau, which the ACC circumvents in Fig. 13a and crosses in Fig. 13b. The third such area is the continental shelf to the northeast from Cape Horn, which pushes the Malvinas Current farther to the east in Fig. 13a. In this experiment, pressure forces balance 51% of the momentum input from wind in the ACC, with the reminder balanced by friction.

Notice that the solutions are strongly affected by the major topographic features (notably the Kerguelen Plateau) despite $F(H)$ depending on H only weakly: $\nabla F = P(-H)\nabla H$. The effect is especially pronounced if $\tau_b \sim u_b$ (Fig. 13a). The sensitivity of the solution to

bottom topography is mainly controlled by the amplitude of the flow near the bottom.

The solution is nearly insensitive to topography for the choice $c_\infty = 0$, $H_0 = 500$ m (cf. Fig. 2f), which confines the flow to the upper ocean. With either parameterization of τ_b the solutions (Fig. 13c, 13d) are quite similar to the solution with a flat-bottom (Fig. 15). The topography plays only a minor role, especially in the case $\tau_b \sim \bar{u}$ (Fig. 13d). Pressure forces balance only 10% of the momentum input from wind in the ACC. We are in the regime $T \sim \varepsilon^{-1}$ (Kamenkovich 1962), where ε may be adjusted to tune the value of the transport. Figure 15 shows that the global scale deviations from zonal path are mainly due to the location of Drake Passage and maximum of the wind stress (see introduction). The results of the numerical experiments are summarized in Table 4. The values of ε in each experiment was selected to yield the correct order of the ACC transport.

Comparing the terms in the vorticity balance (9) we found that the wind forcing is generally at least an order of magnitude smaller than two other terms. Therefore, neglecting ψ_1 in (18) changes the transport by only about 7% and $\psi \approx T\psi_2$. It does not mean, however, that wind forcing is unimportant. Unlike wind-driven models in closed basins, wind stress itself (more precisely, τ/F) is much more important than its curl. For example, if τ/F were constant then $\psi_1 = 0$ everywhere, but the transport T would be proportional to τ/F; cf. (18).

6. Conclusions

A linear equivalent barotropic model with bottom friction is applied to study the effects of the bottom topography H and baroclinicity on the total transport and the position of the ACC. The model is based on the observation by Killworth (1992) who noticed that the time-mean velocity field of the FRAM model is self-similar in the vertical. The parameters of our model are the vertical profile function $P(z)$ and the bottom friction coefficient ε. The vertical profile function $P(z)$ is meant to account for the effect of baroclinicity. The value of ε is chosen so that the model transport is close to observed. The processes of formation of the EB structure are not considered.

Equivalent barotropic models have been previously used in atmospheric weather prediction problems (e.g.,

TABLE 3. Transport (Sv) for the barotropic case with realistic topography.

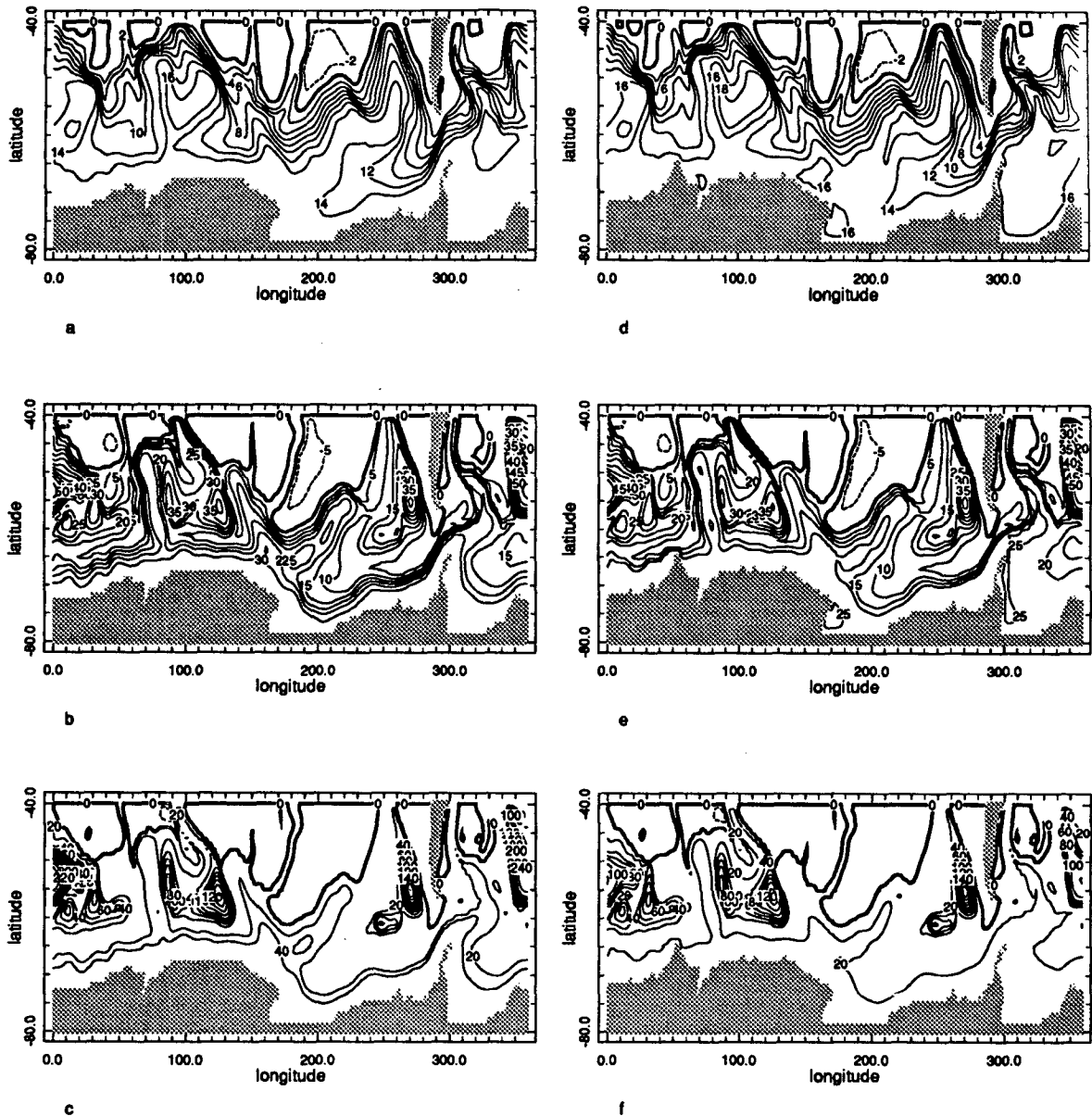| ε (m s^{-1})	Case C	Case B
10^{-2}	16	16
10^{-3}	33	25
10^{-4}	52	28

FIG. 12. The streamfunction ψ for the real topography case. Left column: case C; right column: case B. (a), (d) $\varepsilon = 10^{-2}$ m s^{-1}; (b), (e) ε = 10^{-3} m s^{-1}; (c), (f) $\varepsilon = 10^{-4}$ m s^{-1}. Wind stress is from Hellerman and Rosenstein (1983). The grid resolution is $0.2° \times 0.1°$.

Charney and Eliassen 1949). The application of an EB model to the analysis of the ACC is new. The EB model is relatively simple and formally equivalent to a barotropic model, allowing one to use numerous results previously obtained.

Asymptotic analysis of the model equations for small friction delineates two different asymptotic regimes: (i) If potential vorticity contours that are closed around Antarctica exist, then the ACC transport varies inversely with ε; (ii) if all the potential vorticity contours originate and terminate at the boundaries, then the ACC transport is independent of

friction for small ε. We developed a numerical scheme suitable for solving linear vorticity equations with small bottom friction and some of the potential vorticity contours closed. Computational tests confirmed the analytical results.

A field of large-scale bottom topography in the Antarctic region was constructed by filtering 5' resolution data with a smooth kernel as suggested by Il'in et al. (1974). This procedure yields a smooth topography $\bar{H}$ that closely corresponds to the original.

For the barotropic ocean [$P(z) = 1$] with realistic topography, we considered two cases with slightly
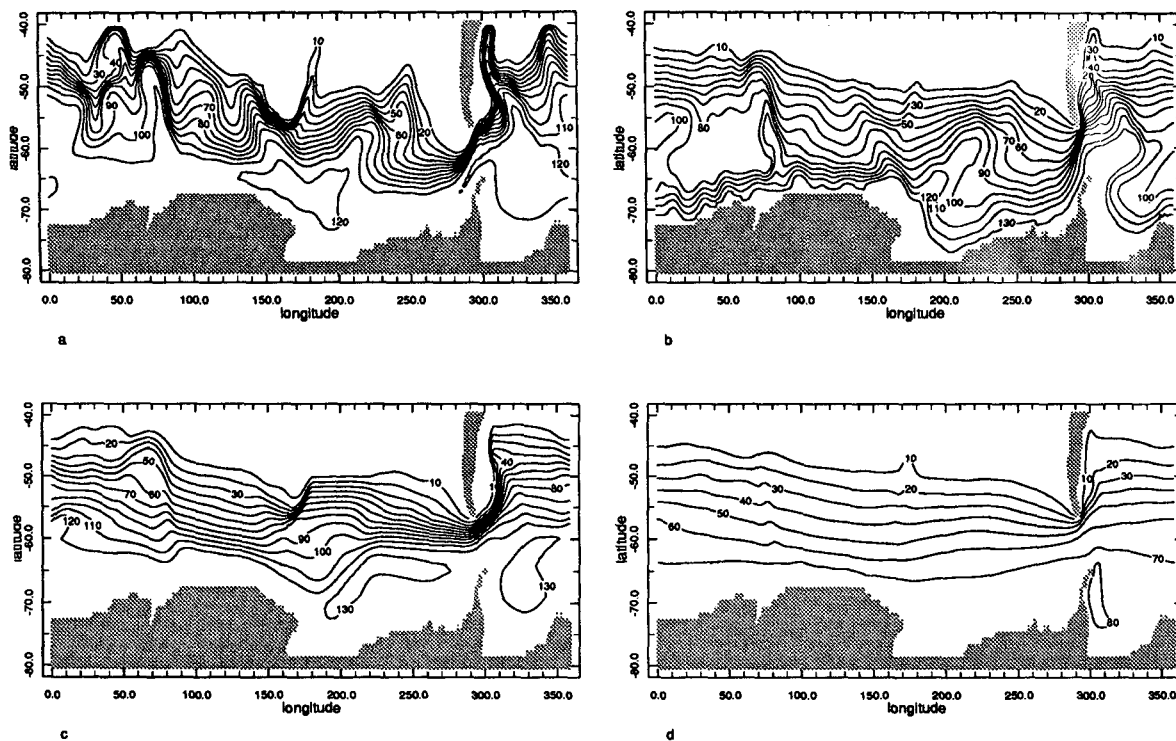
FIG. 13. The streamfunction ψ for the equivalent barotropic model with the vertical structure (24). (a) $c_\infty = 0.05$, $H_0 = 900$ m, τ_b $\sim \mathbf{u}_b$, $\varepsilon = 10^{-2}$ m s^{-1}; (b) $c_\infty = 0.05$, $H_0 = 900$ m, $\tau_b \sim \bar{\mathbf{u}}$, $\varepsilon = 3 \cdot 10^{-3}$ m s^{-1}; (c) $c_\infty = 0$, $H_0 = 500$ m, $\tau_b \sim \mathbf{u}_b$, $\varepsilon = 1$ m s^{-1}; (d) c_∞ $= 0$, $H_0 = 500$ m, $\tau_b \sim \bar{\mathbf{u}}$, $\varepsilon = 10^{-2}$ m s^{-1}. The grid resolution and wind are as in Fig. 12.
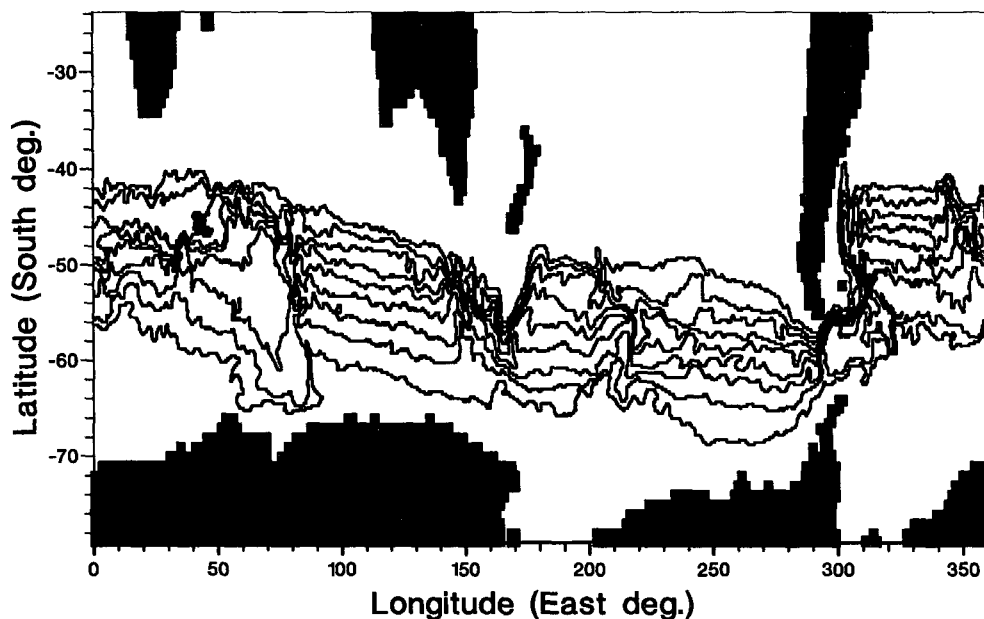

FIG. 14. The time-averaged transport streamlines of the ACC from FRAM (Courtesy V. Ivchenko).
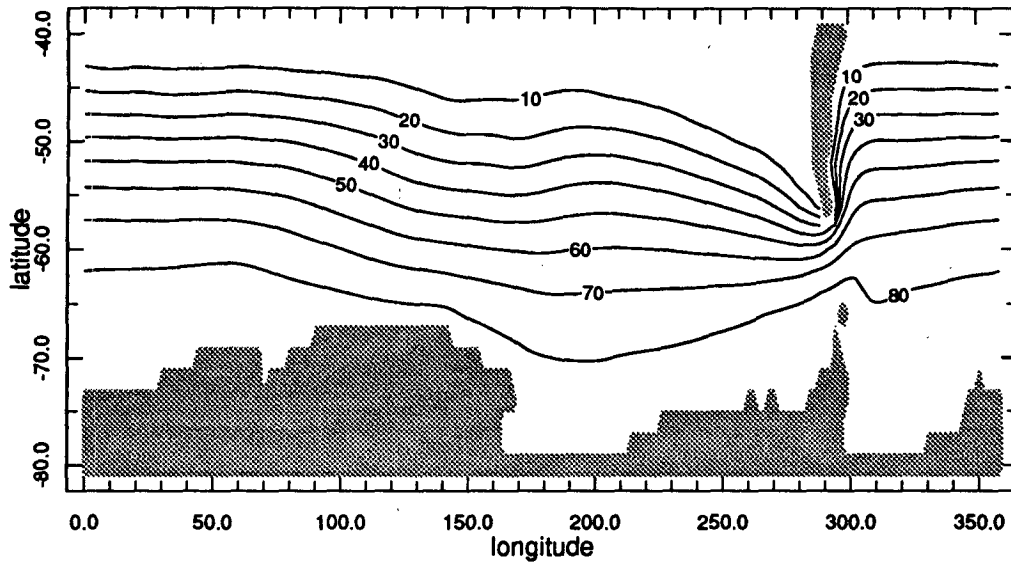
FIG. 15. The streamfunction ψ for the flat-bottom case, $\varepsilon = 10^{-2}$ m s^{-1}. Wind is as in Fig. 12, $c_\infty = 0.05$, $H_0 = 900$ m. The grid resolution is $0.4° \times 0.2°$.

modified coastlines. In one case all potential vorticity contours were blocked; in the other some potential vorticity contours were closed around Antarctica. In the case when all the potential vorticity contours are blocked, the transport is smaller than observed and the realistic transport is impossible, with any friction, on any grid. In the other case, the theory suggests that the transport will vary as ε^{-1}, so the observed transport is achievable. However, the band of potential vorticity contours that are closed around Antarctica is so narrow that it requires very small friction and extremely high resolution. Even if such an experiment were completed, the ACC would be positioned far south of its real path. In addition, the result would not be robust with respect to the perturbations in $\bar{H}$.

We conclude that a linear barotropic model cannot be used to determine the transport and the position of the ACC. We believe that the inclusion of nonlinear terms will not mend the situation.

The vertical profile of the velocity field for the EB model is taken to approximate the time-mean FRAM solution (Killworth 1992). The solution to the EB model reproduces the major features of the time- and depth-averaged FRAM solution reasonably well. The ACC is strongly steered by the major topographic features (e.g., Kerguelen Plateau and the New Zealand Plateau). The comparison with the FRAM solution is much improved by parameterization of the bottom friction via near-bottom velocity, in contrast to the traditional parameterization of bottom friction via vertically averaged velocities. This tends to shut off the flow in the shallow regions (e.g., the New Zealand Plateau or the continental shelf of South America).

We showed that the EB model satisfactorily describes the position and the total transport of the ACC. These are determined by the location of the continents (especially Drake Passage), bottom topography, baroclinicity (parameters c_∞ and H_0 in our model), and the wind stress field.

The EB model is found to be robust with respect to perturbations $\delta \bar{H}$ in the bathymetry field.

The EB model allows calculation of momentum and vorticity balances. In the experiments with the approximate vertical profile of the time-mean FRAM solution, the resultant zonal pressure force (bottom pressure drag plus pressure force against the fluid boundaries) balances a major part of zonal momentum input from wind (62% if $\tau_b \sim u_b$ and 51% if $\tau_b \sim \bar{u}$). The remainder is balanced by frictional terms.

The sensitivity tests show that, if the profile function $P(z)$ quickly decays to zero, friction is much more important in the zonal momentum balance (over 90% in the momentum balance in our test runs). The influence of topography on the current for such profile is minor

TABLE 4. Summary of the numerical experiments with the EB model.

Parameters of P (z) [cf. (24)]	$\tau_b \sim u_b$	$\tau_b \sim \bar{u}$
$c_\infty = 0.05$, $H_0 = 900$ m	$\varepsilon = 10^{-2}$ m s^{-1}, $T = 118$ Sv	$\varepsilon = 3\cdot10^{-3}$ m s^{-1}, $T = 133$ Sv
$c_\infty = 0$, $H_0 = 500$ m	$\varepsilon = 1$ m s^{-1}, $T = 129$ Sv	$\varepsilon = 10^{-2}$ m s^{-1}, $T = 80$ Sv

and streamlines are nearly zonal: it resembles the flat-bottom case.

The role of the parameterization of bottom friction via near-bottom velocities is to shut off the flow in the shallow regions. Comparison with the FRAM solution suggests that this approach yields more realistic results than the traditional parameterization of bottom friction via vertically averaged velocities. The analysis of vorticity balance shows that unlike wind-driven models in closed basins wind stress itself is much more important than its curl.

Thus, the equivalent barotropic model provides a simple way to account for the integral effects of baroclinicity and topography. A proper selection of the vertical profile function $P(z)$ allows to model a wide variety of possible baroclinic structures: from purely barotropic to realistic (e.g., calculated by FRAM) to strongly baroclinic. The solutions presented bear significantly greater resemblance to reality than the barotropic solutions. The EB model proved capable of reproducing reasonably well both the transport and the overall position of the ACC. However, the model gives unsatisfactory results over the regions with steep topography, for example, near southern edge of the Kerguelen Plateau and in the Weddell and Ross gyres where the EB assumption (3) is less likely to hold.

APPENDIX A

Asymptotic Analysis of the Case with Closed q Isolines

To complete the consideration of the case $\delta < 1$ (section 4) we proceed with asymptotic analysis of the problem (see also Kamenkovich 1962; Has'minskii 1962; Gill 1968).

In the coordinates s, q (s is the coordinate along q isolines increasing to the east) (9) can be written as

$$\varepsilon \Lambda \psi + \frac{\partial \psi}{\partial s} = W(s, q), \quad (A1)$$

where

$$\Lambda = a(s, q) \frac{\partial^2}{\partial q^2} + b(s, q) \frac{\partial^2}{\partial q \partial s} + c(s, q) \frac{\partial^2}{\partial s^2} + d(s, q) \frac{\partial}{\partial q} + e(s, q) \frac{\partial}{\partial s}.$$

Here a, b, c, d, e, and W are periodic functions of s ($0 \le s \le 2\pi$) in the interval $q_s < q < q_b$. The solution within the band $q_s < q < q_b$ is sought as an asymptotic series

$$\psi = \frac{1}{\varepsilon} \psi_0(s, q) + \psi_1(s, q) + \varepsilon \psi_2(s, q), \quad (A2)$$

where the ψ_k ($k = 0, 1, 2, \cdots$) are periodic in s. Substituting (A2) in (A1) and collecting terms at powers of ε yields

$$\frac{\partial \psi_0}{\partial s} = 0 \quad (A3)$$

$$\Lambda \psi_0 + \frac{\partial \psi_1}{\partial s} = W \quad (A4)$$

$$\Lambda \psi_1 + \frac{\partial \psi_2}{\partial s} = 0. \quad (A5)$$

Equation (A3) implies $\psi_0 = \psi_0(q)$. Averaging (A4) in s yields an ordinary differential equation for ψ_0:

$$\bar{\Lambda} \psi_0 = \bar{W}(q), \quad (A6)$$

where

$$\bar{\Lambda} = \overline{a(s, q)} \frac{\partial^2}{\partial q^2} + \overline{d(s, q)} \frac{\partial}{\partial q}$$

$$\overline{(\cdots)} = \frac{1}{2\pi} \int_0^{2\pi} (\cdots) ds.$$

Thus, we have an ordinary differential equation for ψ_0. The next approximation is found from (A4) as

$$\psi_1(s, q) = \int_0^s (W - \Lambda \psi_0) ds' + \psi_1^{(0)}(q). \quad (A7)$$

The ordinary differential equation for $\psi_1^{(0)}$ is obtained from averaging (A5) in s:

$$\bar{\Lambda} \psi_1^{(0)} = -\overline{\Lambda \int_0^s (W - \Lambda \psi_0) ds'}, \quad (A8)$$

and so on.

The boundary conditions at the northern boundary $q = q_b$ are determined from the continuity of ψ and $\partial \psi / \partial q$. The solution in the vicinity of $q = q_b$ is sought as

$$\psi = \psi_{sv}(s, q) + \varepsilon^{-1/2} \varphi_0^+(\xi, s) + \cdots, \xi > 0 \quad (A9)$$

$$\psi = \varepsilon^{-1} \psi_0(q) + \varepsilon^{-1/2} \varphi_0^-(\xi, s) + \cdots, \xi < 0, \quad (A10)$$

where ψ_{sv} is the known solution in the region with blocked q isolines and

$$\xi = \frac{q - q_b}{\varepsilon^{1/2}}. \quad (A11)$$

Substituting (A9)–(A11) in (A1) yields to leading order

$$a(s, q_b) \frac{\partial^2 \varphi_0^+}{\partial \xi^2} + \frac{\partial \varphi_0^+}{\partial s} = 0 \qquad \text{(A12)}$$

$$a(s, q_b) \frac{\partial^2 \varphi_b^-}{\partial \xi^2} + \frac{\partial \varphi_0^-}{\partial s} = 0. \qquad \text{(A13)}$$

The continuity of ψ and $\partial \psi / \partial q$ at $q = q_b$ implies

$$\psi_0(q_b) = 0 \qquad \text{(A14)}$$

$$\left. \frac{\partial \varphi_0^+}{\partial \xi} \right|_{\xi=0} = \left. \frac{\partial \psi_0}{\partial q} \right|_{q=q_b} + \left. \frac{\partial \varphi_0^-}{\partial \xi} \right|_{\xi=0}. \qquad \text{(A15)}$$

The additional boundary conditions needed to determine φ_0^+ and φ_0^- are

$$\varphi_0^+ \to 0 \quad \xi \to \infty \qquad \text{(A16)}$$

$$\varphi_0^- \to 0 \quad \xi \to -\infty \qquad \text{(A17)}$$

$$\varphi_0^+(\xi, s) = 0 \qquad \text{(A18)}$$

at the eastern coast of the meridional barrier

$$\varphi_0^-(\xi, 0) = \varphi_0^-(\xi, 2\pi). \qquad \text{(A19)}$$

In the next order the continuity of ψ at $q = q_b$ implies

$$\varphi_0^+ = \varphi_0^-. \qquad \text{(A18)}$$

If the southern boundary of the domain of closed q contours is fluid (as is the case when $\delta < 1$), then the boundary conditions for ψ_0, φ_0^+, φ_0^- at $q = q_s$ are determined in a way similar to described above. If the southern boundary of the domain of closed q contours is solid (as in the case of the Gill problem) then

$$\psi_0(q_s) = 0 \qquad \text{(A19)}$$

and there is no need to introduce functions φ_k^+, φ_k^-. Thus, the leading order interior solution ψ_0 is found from (A6), (A14), and (A19).

<center>APPENDIX B</center>

The Numerical Scheme

We would like to have a numerical scheme with constant grid spacing capable of reproducing the solution of (9) for small ε, at least outside the boundary layers for moderate space resolutions. This turns out to be a difficult problem. It is known that, when the friction is small, centered finite differences in terms with first derivatives yield spuriously oscillating solutions if the resolution is not sufficient to resolve the boundary layers (e.g., Il'in 1969). Upwind differences, on the other hand, yield smooth solutions at the expense of adding artificial viscosity, which could be larger than the physical one. In the case $\delta = 1.5$, we use the scheme suggested by Il'in (1969) where Eq. (9) written in the form

$$\varepsilon(\psi_{xx} + \psi_{yy}) + a(x, y)\psi_x$$

$$+ b(x, y)\psi_y = f(x, y) \qquad \text{(B1)}$$

is approximated at the point (x_i, y_j) as

$$\varepsilon_{ij}^x \frac{\psi_{i+1,j} - 2\psi_{ij} + \psi_{i-1,j}}{h_x^2} + a_{ij} \frac{\psi_{i+1,j} - \psi_{i-1,j}}{2h_x}$$

$$+ \varepsilon_{ij}^y \frac{\psi_{i,j+1} - 2\psi_{ij} + \psi_{i,j-1}}{h_y^2} + b_{ij} \frac{\psi_{i,j+1} - \psi_{i,j-1}}{2h_y}$$

$$= f(x_i, y_j),$$

where

$$a_{ij} = a(x_i, y_j), \quad b_{ij} = b(x_i, y_j)$$

$$\varepsilon_{ij}^x = \frac{a_{ij}h_x}{2} / \tanh\left(\frac{a_{ij}h_x}{2\varepsilon}\right); \quad \varepsilon_{ij}^y = \frac{b_{ij}h_y}{2} / \tanh\left(\frac{b_{ij}h_y}{2\varepsilon}\right).$$

Here h_x and h_y are the grid sizes in x and y. For fixed h and $\varepsilon \to 0$, the coefficients of the Il'in scheme approach those of the upwind difference scheme, but this scheme is superior to the upwind scheme for several reasons. Like the upwind scheme, this scheme preserves the maximum principle for (B1) (Il'in 1969). However, it is second order in h for fixed ε and for the one-dimensional problem it yields a first-order approximation uniformly in ε, which is not true of the upwind scheme (Il'in 1969). In fact, the scheme is designed in such a way that for a one-dimensional problem with constant $a(x)$ the solution of the discretized equations coincides with the exact solution of the two-point Dirichlet problem on the grid no matter how coarse it is. Therefore, even if $\varepsilon_{ij} \gg \varepsilon$, the increase in the coefficients of the second derivatives in the finite difference equations cannot simply be interpreted as artificial viscosity.

For the Gill problem and in the case $\delta = 0.5$, we apply a hybrid scheme whereby centered differences are used at each grid point laying on a closed q contours (to the south of the barrier for the Gill problem); elsewhere we use the Il'in scheme. The corresponding linear system is solved by the Gauss–Seidel algorithm at points where the Il'in scheme was used and by successive under-relaxation elsewhere. The latter is a slow but stable process that was found appropriate for inverting ill-conditioned matrices resulting from the described scheme.

Let us show using a simple example that in the case of closed q contours centered differences yield nonoscillatory solutions. (Our numerical experiments confirmed this in all situations.) Consider the equation

$$\varepsilon\nabla^2\psi + J(\psi, q) = 1, \qquad \text{(B2)}$$

where

$$q = \alpha y - x. \qquad \text{(B3)}$$

The periodic in s (the coordinate along q isolines) solution to (B2), satisfying the boundary conditions

$$\psi|_{q=0} = \psi|_{q=1} = 0, \qquad \text{(B4)}$$

is

$$\psi = \frac{q(q-1)}{2\varepsilon(1+\alpha^2)} . \qquad (B5)$$

Assuming a uniform grid resolution h in both x and y, the function $\psi(x, y)$ can be represented on the grid as $\psi(ih, jh)$, where i and j are the numbers of grid points in x and y, respectively. Thus, the exact solution on the grid in the interval $0 \le q \le 1$ can be written as

$$\psi\mid_{grid} = \frac{(\alpha jh - ih)(\alpha jh - ih - 1)}{2\varepsilon(1+\alpha^2)} . \qquad (B6)$$

Substitution of (B6) in the finite difference analog of (B2) where first derivatives are approximated by centered differences shows that (B6) is an exact solution of the finite difference equation.

For the Gill problem, the solution obtained using the hybrid scheme was found to be almost identical to that obtained by using Il'in scheme at all points, as in the case $\delta > 1$. The applicability of the Il'in scheme for the Gill problem is somewhat fortuitous and is due to the fact that $\varepsilon_{ij}^y = \varepsilon$ because $b(x, y) = 0$. Our experiments have shown that in the case $\delta = 0.5$ this scheme behaves like an upwind scheme and yields erroneous solutions (see Brandt and Yavneh 1991). A scheme without artificial viscosity in the direction of ∇q is needed in the region of closed characteristics. This is why the hybrid scheme is suggested. One might make a coordinate transformation and apply the Il'in scheme everywhere, but for the real case it would be cumbersome and the hybrid scheme is preferable.

REFERENCES

Bogden, P. S., R. E. Davis, and R. Salmon, 1993: The North Atlantic Circulation: Combining simplified dynamics with hydrographic data. *J. Mar. Res.,* **51,** 1–52.

Brandt, A., and I. Yavneh, 1991: Inadequacy of first-order upwind difference scheme for some recirculating flows. *J. Comput. Phys.,* **93,** 128–143.

Bryan, K., and M. D. Cox, 1972: The circulation of the World Ocean: A numerical study. Part I, A homogeneous model. *J. Phys. Oceanogr.,* **2,** 319–335.

Bye, J. A. T., and T. W. Sag, 1972: A numerical model for circumpolar in a homogeneous world ocean. *J. Phys. Oceanogr.,* **2,** 305–318.

Charney, J. G., and A. Eliassen, 1949: A numerical method for predicting the perturbations of midlatitude westerlies. *Tellus,* **1,** 38–54.

FRAM Group, 1991: An eddy-resolving model of the Southern Ocean. *Eos, Trans. Amer. Geophys. Union,* **72,** 169–175.

Gill, A. E., 1968: A linear model of the Antarctic circumpolar current. *J. Fluid Mech.,* **32,** 465–488.

Gordon, A. L., E. Molinelli, and T. Baker, 1978: Large-scale relative dynamic topography of the Southern Ocean. *J. Geophys. Res.,* **83**(C6), 3023–3032.

Grose, T. J., J. A. Johnson, and G. R. Bigg, 1995: A comparison between the FRAM (Fine Resolution Antarctic Model) results and observations in the Drake Passage. *Deep-Sea Res.,* **42,** 365–388.

Has'minskii, R. Z., 1962: On certain differential equations encountered in the investigation of oscillations with small random perturbations. *Dokl. Akad. Nauk SSSR,* **142,** 125–129 (Translated from Russian).

Hellerman, S., and M. Rosenstein, 1983: Normal monthly wind stress over World Ocean with error estimates. *J. Phys. Oceanogr.,* **13,** 1093–1104.

Hidaka, K., and M. Tsuchiya, 1953: On the Antarctic Circumpolar Current. *J. Mar. Res.,* **12,** 214–222.

Il'in, A. M., 1969: Finite difference scheme for differential equation with small parameter at the highest order derivative. *Mathematical Notes,* **6,** 237–248, (Translated from Russian).

——, 1992: Matching of asymptotic expansions of solutions of boundary value problems. Amer. Math. Soc., 281 pp., (Translated from Russian).

——, V. M. Kamenkovich, T. G. Zhugrina, and M. M. Silkina, 1969: On the calculation of the total transports in the World Ocean. *Physics of Atmosphere and Ocean,* **5,** 1160–1171, (Translated from Russian).

——, ——, V. F. Kanayev, T. G. Zhugrina, and L. I. Lavrishcheva, 1974: An experiment in constructing a smoothed bottom relief of the World Ocean. *Okeanologiya,* **14,** 617–622, (Translated from Russian).

——, ——, and T. G. Zhugrina, 1974: Seasonal variability of a depth-averaged circulation in the World Ocean. *Okeanologiya,* **14,** 770–780, (Translated from Russian).

Ishida, A., 1994: Effects of partial meridional barriers on the Antarctic Circumpolar Current—wind-driven barotropic model. *Dyn. Atmos. Oceans,* **20,** 315–341.

Ivanov, Y. A., and V. M. Kamenkovich, 1959: Bottom relief as a basic factor contributing to the lack of zoning in the Antarctic Circumpolar Current. *Dokl. Akad. Nauk SSSR,* **128,** 977–979, (Translated from Russian).

Ivchenko, V. O., K. J. Richards, and D. P. Stevens, 1996: The dynamics of the Antarctic Circumpolar Current. *J. Phys. Oceanogr.,* **26,** 753–774.

Johnson, J. A., and R. B. Hill, 1975: A three-dimensional model of the Southern Ocean with bottom topography. *Deep-Sea Res.,* **22,** 745–751.

Kamenkovich, V. M., 1960: The influence of bottom relief on the Antarctic Circumpolar Current. *Dokl. Akad. Nauk SSSR,* **134,** 983–984, (Translated from Russian).

——, 1961: The integration of the marine current theory equations in multiply connected regions (in Russian.) *Dokl. Akad. Nauk SSSR,* **138,** 629–631, (Translated from Russian).

——, 1962: On the theory of the Antarctic Circumpolar Current. *Trudy Instituta Okeanologii,* **56,** 245–306, (Translated from Russian).

——, and G. M. Reznik, 1972: Bottom topography-induced detachment of the boundary current from the shore (linear barotropic model). *Dokl. Akad. Nauk SSSR,* **202,** 16–18 (Translated from Russian).

——, M. Cane, A. Krupitsky, and N. Naik, 1994: On the influence of bottom topography on the Antarctic Circumpolar Current transport. *Annales Geophysicae,* European Geophysical Society. Part II. Oceans, Atmosphere, Hydrology and Nonlinear Geophysics. Suppl. II to Vol. 12, EGS, p. C222.

Killworth, P. D., 1992: An equivalent barotropic mode in the Fine Resolution Antarctic Model. *J. Phys. Oceanogr.,* **22,** 1379–1387.

——, and M. M. Nanneh, 1994: Isopycnal momentum budget of the Antarctic Circumpolar Current in the Fine Resolution Antarctic Model. *J. Phys. Oceanogr.,* **24,** 1201–1223.

Krupitsky, A., 1995: Local and remote forcing of the barotropic transport through a periodic gap in a basin with bottom topography. *J. Mar. Res.,* **53,** 201–210.

——, and M. Cane, 1994: On topographic pressure drag in a zonal channel. *J. Mar. Res.,* **52,** 1–22.

Laykhtman, D. L., B. A. Kagan, L. A. Oganesyan, and R. V. Pyaskovsky, 1971: Global circulation in a barotropic ocean of variable depth. *Dokl. Akad. Nauk SSSR,* **198,** 1–3.

Marshall, D., 1995: Topographic steering of the Antarctic Circumpolar Current. *J. Phys. Oceanogr.,* **25,** 1636–1650.

McCartney, M. S., 1976: The interaction of the zonal currents with topography with application to the Southern Ocean. *Deep-Sea Res., 23,* 413–427.

McWilliams, J. C., W. R. Holland, and J. H. S. Chow, 1978: A description of numerical Antarctic Circumpolar Currents. *Dyn. Atmos. Oceans, 2,* 213–291.

Munk, W. H., and E. Palmen, 1951: Note on the dynamics of the Antarctic Circumpolar Current. *Tellus, 3,* 53–55.

Orsi, A., T. Whitworth III, and W. Nowlin Jr., 1995: On the meridional extent and fronts of the Antarctic Circumpolar Current. *Deep-Sea Res., 42,* 641–673.

Schröter, J., and C. Wunsch, 1986: Solution of nonlinear finite difference ocean models by optimization methods with sensitivity and observational strategy analysis. *J. Phys. Oceanogr., 16,* 1855–1874.

Shtockman, V. B., 1950: Determination of current velocities and density distribution in a cross-section of an infinite rotating channel in terms of the wind effect and lateral friction (Opredelenie skorostei techeniya i raspredeleniya plotnosti v poperechnom sechenii beskonechnogo kanala v zavisimosti ot effecta vetra i bokovogo treniya v pole sily Koriolisa.) *Dokl. Akad. Nauk SSSR,* LXXI, (No. 1), 41–44, (In Russian).

Smith, N., and C. Fandry, 1978: Combined effects of wind stress and topography in a two layer model of the Southern Ocean. *Deep-Sea Res., 25,* 371–390.

Stommel, H., 1957: A survey of ocean current theory. *Deep-Sea Res., 4,* 149–184.

Thompson, R. O. R. Y., 1971: Structure of the Antarctic Circumpolar Current. *J. Geophys. Res., 76,* 8694.

Welander, P., 1968: Wind-driven circulation in one and two-layer oceans of variable depth. *Tellus, 20,* 1–15.

Wang, L., 1994: A linear homogeneous channel model for topographic control of the Antarctic Circumpolar Current. *J. Mar. Res., 52,* 649–685.

——, and R. X. Huang, 1995: A linear homogeneous model of wind-driven circulation in a β-plane channel. *J. Phys. Oceanogr., 25,* 587–603.

Whitworth, T., III, 1983: Monitoring the transport of the Antarctic Circumpolar Current in Drake Passage. *J. Phys. Oceanogr., 13,* 2045–2057.

Wolff, J.-O., and D. J. Olbers, 1989: The dynamical balance of the Antarctic Circumpolar Current studied with an eddy resolving quasi-geostrophic model. *Mesoscale-Synoptic Coherent Structures in Geophysical Turbulence,* J. C. J. Nihoul and B. M. Jamart, Eds., Elsevier, 435–458.